Journal of Computational Physics 228 (2009) 8919–8943

Contents lists available at ScienceDirect

Journal of Computational Physics

journal homepage: www.elsevier.com/locate/jcp

A numerical method for solving the Vlasov–Poisson equation based on the conservative IDO scheme

Kenji Imadera [a,*], Yasuaki Kishimoto [a], Daisuke Saito [a], Jiquan Li [a], Takayuki Utsumi [b]

[a] Department of Fundamental Energy Science, Graduate School of Energy Science, Kyoto University, Gokasho, Uji, Kyoto 611-0011, Japan
[b] Department of Electronics and Computer Science, Tokyo University of Science, Yamaguchi, 1-1 Daigaku-dori, Sanyou-Onoda, Yamaguchi 756-0884, Japan

ARTICLE INFO

Article history:
Received 19 March 2009
Received in revised form 7 August 2009
Accepted 3 September 2009
Available online 11 September 2009

Keywords:
Vlasov–Poisson simulation
Fokker–Planck simulation
IDO scheme
Conservative form
Entropy production

ABSTRACT

We have applied the conservative form of the Interpolated Differential Operator (IDO-CF) scheme in order to solve the Vlasov–Poisson equation, which is one of the multi-moment schemes. Through numerical tests of the nonlinear Landau damping and two-stream instability, we compared the present scheme with other schemes such as the Spline and CIP ones. We mainly investigated the conservation property of the L1-norm, energy, entropy and phase space area for each scheme, and demonstrated that the IDO-CF scheme is capable of performing stable long time scale simulation while maintaining high accuracy. The scheme is based on an Eulerian approach, and it can thus be directly used for Fokker–Planck, high dimensional Vlasov–Poisson and also guiding-center drift simulations, aiming at particular problems of plasma physics. The benchmark tests for such simulations have shown that the IDO-CF scheme is superior in keeping the conservation properties without causing serious phase error.

1. Introduction

The Vlasov equation describes the evolution of the distribution function in phase space in collisionless plasmas with no dissipation. The Vlasov–Maxwell and/or the Vlasov–Poisson equation system have been intensively investigated in studying various linear and nonlinear plasma dynamics where kinetic effects such as wave–particle interaction play an important role [1–4]. Contrary to a particle approach such as Particle-In-Cell method [3,4], the Vlasov approach, which directly solves the distribution function by discretizing the phase space, requires a large amount of computer resources, especially when the dimension of the phase space becomes higher. However, the Vlasov approach is superior in reducing numerical noise compared with the particle one. Furthermore, it is easier to introduce dissipation such as collision as well as source/sink terms, which are important in studying long time scale plasma dynamics as an open system. Because of these advantages, the Vlasov approach has become widely accepted in such researches as magnetically confined fusion plasmas [5–8], laser produced plasmas [9], astrophysical plasmas [10], etc.

Several numerical schemes have been developed for solving the Vlasov equation. Cheng and Knorr [11] originally introduced a splitting scheme which solves the Vlasov equation based on the Semi-Lagrangian approach by separating the convection dynamics along each coordinate in phase space. This scheme belongs to one of the explicit symplectic time integrations [12] which ensure the conservation of system energy. However, numerical diffusion originating from the interpolation of the physical quantities among grids is another problem. Recently, the CIP (Constrained Interpolation Profile) scheme [13,14], in which not only the distribution function f, but also its phase space derivatives, i.e., $\partial f/\partial x$ and $\partial f/\partial v$

* Corresponding author. Tel.: +81 774 38 4441; fax: +81 774 32 9397.
E-mail address: imadera@center.iae.kyoto-u.ac.jp (K. Imadera).

0021-9991/$ - see front matter © 2009 Elsevier Inc. All rights reserved.
doi:10.1016/j.jcp.2009.09.008

are traced, has been applied for solving the Vlasov–Poisson equation system by incorporating it with the splitting scheme [15]. This scheme is efficient in reducing numerical diffusion while keeping the third-order numerical accuracy. As a result, a small number of mesh points can successfully reproduce the fundamental phase space dynamics like particle trapping and associated vortex formation with high accuracy. However, the scheme is hardly applied to a problem that includes dissipation and/or source/sink terms due to the nature of the Semi-Lagrangian approach. Furthermore, when the convection velocity is a function of a configuration space coordinate such as $\vec{E} \times \vec{B}$ motion in plasmas, a phase error associated with the convection was found to occur [16].

Recently, an alternative approach referred to as the IDO (Interpolated Differential Operator) scheme [17,18] has been developed in the CFD (Computational Fluid Dynamics) field. In this scheme, physical quantities, such as density, velocity, etc., are replaced by local interpolation functions determined from those values and their spatial derivatives on each grid point, so that the differential operators in fluid equations are analytically treated. Then, time integration can be performed based on an Eulerian approach such as the Runge–Kutta method. The IDO scheme has been applied to various CFD problems and found to be efficient in capturing a fine scale structure in multi-dimensional fluid problems [19]. Furthermore, a conservative counterpart referred to as the IDO-CF scheme [20], which uses the integrated values of the physical quantities to determine the interpolation function, has been developed. This scheme ensures rigorous conservation for the integrated value over the whole system, so that it can be applied it to the problems that require long time scale simulation. The IDO-CF scheme is close to the conservative PSM scheme [21] which solve the equation as an integral form by using the line-integrated values, although the integrated values do not time-integrated as an independent variable in the PSM scheme.

Based on these advantages in multi-moment schemes, we here, for the first time, introduce the IDO-CF scheme for the Vlasov–Poisson equation system. The distribution function in phase space is now replaced by local interpolation functions along each coordinate in phase space, so that the convection and acceleration terms in the Vlasov equation are analytically discretized. In the IDO-CF scheme, the total particle number is rigorously conserved by using the line-integrated and also cell-integrated values in constructing the interpolation function. Based on this scheme, we have developed a Vlasov code which is one-dimensional (1D) in configuration space and 1D in velocity one, and applied it to the problems of the nonlinear Landau damping and two-stream instability. We have investigated the conservation property of the scheme in terms of the L1-norm, energy, entropy and phase space area through comparison with other schemes such as Spline and CIP ones. Note that the conservation of the phase space area is a direct consequence of the Liouville theorem for the distribution function in Hamiltonian dynamics, and the entropy is a measure of the higher order moment related to the fine scale structure in phase space.

The IDO-CF scheme shows excellent stability and is highly accurate in maintaining the conservation of the L1-norm and total energy over many bounce periods of trapped particles. On the other hand, the entropy and phase space area increase by a certain amount in all schemes during the initial trapping phase and coalescence process of vortices where complicated stretching and folding dynamics of distribution function take place [22–24]. Such increase originates from the vortex formation in phase space and associated trapping dynamics of particles due to a finite amplitude wave. Namely, during this process, infinitesimally small numerical dissipation causes stochastic motion of particles near the separatrix so that a coarse-grained distribution function is created [25]. Such an ergotization corresponds to the increase of the entropy and phase space area. Once such a distribution is established, the increases of the entropy and phase space area saturate and tend to converge to asymptotic values. This state is considered to be a quasi-stable BGK solution [1]. It has been pointed out that the microscopic resolution influences the macroscopic dynamics [26,27].

In order to study this aspect, we have performed a simulation that imposes a symmetric constraint to the initial distribution by keeping only even parity modes and investigated how the symmetric structure in phase space $f(x, v) = f(-x, -v)$ is preserved during the simulation [9]. It was found that the symmetric structure is precisely kept even after complex vortex merging, which is accompanied by the increase of entropy, takes place. This suggests that the ergotization process does not directly influence the symmetry of the distribution function, which is one of the most primitive macroscopic dynamics.

The IDO-CF scheme can be straightforwardly extended to a simulation including dissipation and also sink/source terms since the scheme is based on an Eulerian approach. As an example, we have performed a simulation which includes the collisional effect. In this simulation, the entropy increases physically, and the L1-norm and energy remain almost constant due to the smoothing of the distribution function, which effectively increases the numerical accuracy for a given mesh size.

Moreover, it can be also extended to high dimensional Vlasov–Poisson simulations even when the velocity depends on configuration space coordinates. As benchmark tests for such simulations, we have performed a 4D Vlasov–Poisson simulation in phase space and also a 2D guiding-center drift simulation in real space where the velocity depends on the spatial coordinate via $\vec{E} \times \vec{B}$ drift motion. In these cases, the linear growth rate is well in agreement with the theoretical one, and the conserved quantities such as mass, energy and enstrophy are kept almost constant without causing serious phase error.

The reminder of this paper is organized as follows. In Section 2, we briefly describe the IDO-CF scheme and apply it to the two-dimensional Vlasov–Poisson equation system. In Section 3, we present the numerical results of the nonlinear Landau damping and two-stream instability, and discuss the numerical accuracy and stability from the view point of long time scale simulation. The present scheme is then applied to a Fokker–Planck, a high dimensional Vlasov–Poisson and also a guiding-center drift simulations, aiming at particular problems of plasma physics in Section 4. Finally, the concluding remarks are given in Section 5.

2. IDO-CF scheme and its application to the Vlasov–Poisson equation system

In Section 2.1, we briefly review the IDO-CF scheme [20] which has been applied in the CFD field. In Section 2.2, we then introduce this scheme to solve the Vlasov–Poisson equation system in two-dimensional phase space (x, v). Here, we have adopted two numerical methods to evaluate the nonlinear terms in the Vlasov–Poisson equation system.

2.1. IDO-CF scheme

Here, we explain the formalism of the IDO-CF scheme based on a simple 1D advection equation:

$$\frac{\partial f(t,x)}{\partial t}+\frac{\partial\{uf(t,x)\}}{\partial x}=0, \tag{1}$$

where u is the convection velocity which satisfies $du/dx=0$. The space x and function $f(x)$ are discretized as $x_i=i\Delta x$, and $f_i=f(x_i)$ with an equal mesh size $\Delta x=L_x/N_x$, where L_x and N_x are the spatial periodic length and the number of mesh points, respectively. In the conventional non-conservative IDO scheme, i.e., IDO-NCF scheme [17], the interpolation function of $f(x)$ between x_i and x_{i+1} is constructed via a cubic Hermitian polynomial function as

$$F(x;f_i,f_{i+1},f_{x;i},f_{x;i+1})=a(x-x_i)^3+b(x-x_i)^2+c(x-x_i)+d, \tag{2}$$

where the coefficients are determined from the four conditions as $F(x_i)=f_i$, $F(x_{i+1})=f_{i+1}$, $(\partial F(x)/\partial x)_{x=x_i}=f_{x;i}$ and $(\partial F(x)/\partial x)_{x=x_{i+1}}=f_{x;i+1}$.

On the other hand, in the IDO-CF scheme, instead of the derivative values at grid points, we introduce cell-integrated values between x_i and x_{i+1} given by

$$\rho_{i+\frac{1}{2}}=\int_{x_i}^{x_{i+1}}f(x)dx, \tag{3}$$

and employ the value to construct the interpolation function as

$$F(x;f_i,f_{i+1},\rho_{i+\frac{1}{2}})=a_+(x-x_i)^2+b_+(x-x_i)+c_+. \tag{4}$$

Here, $F(x)$ is the quadratic function and the coefficients are determined by using three conditions,

$$F(x_i)=f_i, \tag{5}$$

$$F(x_{i+1})=f_{i+1}, \tag{6}$$

$$\int_{x_i}^{x_{i+1}}F(x)dx=\rho_{i+\frac{1}{2}}, \tag{7}$$

as follows:

$$\begin{cases} a_+=\dfrac{3(f_i+f_{i+1})}{\Delta x^2}-\dfrac{6\rho_{i+\frac{1}{2}}}{\Delta x^3} \\ b_+=-\dfrac{2(2f_i+f_{i+1})}{\Delta x}+\dfrac{6\rho_{i+\frac{1}{2}}}{\Delta x^2} \\ c_+=f_i. \end{cases} \tag{8}$$

When $u<0$, namely, the profile $f(x)$ is convected to the negative x-direction, we utilize this interpolation function for the upwind discretization of spatial derivatives as

$$f_{x;i}=\left.\frac{\partial f}{\partial x}\right|_{x=x_i}\simeq\frac{\partial}{\partial x}F(x;f_i,f_{i+1},\rho_{i+\frac{1}{2}})|_{x=x_i}. \tag{9}$$

In the case of $u>0$, we interpolate the distribution function to the positive x-direction as

$$F(x;f_i,f_{i-1},\rho_{i-\frac{1}{2}})=a_-(x-x_i)^2+b_-(x-x_i)+c_-, \tag{10}$$

where

$$\begin{cases} a_-=\dfrac{3(f_i+f_{i-1})}{\Delta x^2}-\dfrac{6\rho_{i-\frac{1}{2}}}{\Delta x^3} \\ b_-=\dfrac{2(2f_i+f_{i-1})}{\Delta x}-\dfrac{6\rho_{i-\frac{1}{2}}}{\Delta x^2} \\ c_-=f_i, \end{cases} \tag{11}$$

and evaluate the spatial derivative by using Eq. (10) instead of Eq. (4). Then, the time derivatives of the distribution function and its cell-integrated value are determined as

$$f_{t;i}=-uf_{x;i}, \tag{12}$$

$$\rho_{t;i+\frac{1}{2}}=-u(f_{i+1}-f_i). \tag{13}$$

According to Eqs. (12) and (13), we can time-integrate these two variables by using some numerical procedures such as the Runge–Kutta method. Note that Eq. (13) is expressed as a flux form, so that $\sum_{i=1}^{N_x}\rho_{i+\frac{1}{2}}$ is rigorously conserved. In Ref. [20], the Fourier analysis of the IDO-CF scheme coupled with the Runge–Kutta scheme is performed to evaluate the stability and accuracy. The IDO-CF scheme provides accurate phase for a wide range of wave numbers, and gives less dissipative solutions than the third-order upwind finite difference scheme (FDM). Thus the present scheme is superior in investigating the problems that require a long time scale simulation. On the other hand, the CFL condition is limited in a finite Courant number same as the other Enlerian schemes. For example, the Courant number is estimated as 0.42 in the case of the 1D advection equation to which the second-order upwind IDO-CF and the fourth-order Runge–Kutta schemes are applied.

2.2. Application of the IDO-CF scheme to the Vlasov–Poisson equation system

We applied the IDO-CF scheme to the Vlasov–Poisson equation system, which is the advection equation of the distribution function in phase space. Here, we consider a simple two-dimensional phase space (x, v), i.e., 1D in configuration space and also 1D in velocity one. In this case, the normalized forms of the Vlasov–Poisson equation system are described as follows:

$$\frac{\partial f(t,x,v)}{\partial t}+\frac{\partial\{vf(t,x,v)\}}{\partial x}-\frac{\partial\{E(t,x)f(t,x,v)\}}{\partial v}=0, \tag{14}$$

$$\frac{\partial E(t,x)}{\partial x}=-\left\{\int_{-\infty}^{\infty}f(t,x,v)dv-1\right\}, \tag{15}$$

where $dv/dx=0$ and $dE(x,t)/dv=0$ are satisfied. The Vlasov equation can be seen as the continuity equation for the distribution function transported by incompressible Hamiltonian flows in phase space so that the IDO-CF scheme can be directly applied to this system. Here, a rectangular mesh is used to discretize the phase space with the computational domain $R=\{(x,v)\,|\,|x|\leqslant 0.5L_x, |v|\leqslant V_{max}\}$, when L_x is the spatial periodic length and V_{max} is the cutoff velocity. The space x, velocity v and function $f(x,v)$ were discretized as $x_i=-0.5L+i\Delta x$, $v_j=-V_{max}+j\Delta v$ and $f_{i,j}=f(x_i,v_j)$ with an equal mesh size $\Delta x=L_x/N_x$ and $\Delta v=2V_{max}/N_v$, where N_x and N_v are the number of mesh points used along the x and v directions, respectively. The discretization forms of the two-dimensional Vlasov equation and its line/cell-integrated ones are given as follows:

$$f_{t;i,j}=-v_j f_{x;i,j}+E_i f_{v;i,j}, \tag{16}$$

$$\rho_{t;i+\frac{1}{2}j}=-v_j\left(f_{i+1\,j}-f_{i,j}\right)+\int_{x_i}^{x_{i+1}}E(x)f_v(x,v_j)dx, \tag{17}$$

$$\zeta_{t;i,j+\frac{1}{2}}=-\int_{v_j}^{v_{j+1}}vf_x(x_i,v)dv+E_i\left(f_{i,j+1}-f_{i,j}\right), \tag{18}$$

$$M_{t;i+\frac{1}{2}j+\frac{1}{2}}=-\int_{v_j}^{v_{j+1}}vf(x_{i+1},v)dv+\int_{v_j}^{v_{j+1}}vf(x_i,v)dv+\int_{x_i}^{x_{i+1}}E(x)f(x,v_{j+1})dx-\int_{x_i}^{x_{i+1}}E(x)f(x,v_j)dx, \tag{19}$$

where we define the line-integrated value along the x and v directions as

$$\rho_{i+\frac{1}{2}j}=\int_{x_i}^{x_{i+1}}f(x,v_j)dx, \tag{20}$$

$$\zeta_{i,j+\frac{1}{2}}=\int_{v_j}^{v_{j+1}}f(x_i,v)dv, \tag{21}$$

and also the cell-integrated one as

$$M_{i+\frac{1}{2}j+\frac{1}{2}}=\int_{v_j}^{v_{j+1}}\int_{x_i}^{x_{i+1}}f(x,v)dx\,dv. \tag{22}$$

The electric field on each mesh point $E_i=E(x_i)$ is determined from the discretized poisson equation:

$$\frac{\phi_{i+1}-2\phi_i+\phi_{i-1}}{\Delta x^2}=\sum_{j=0}^{N_v}\zeta_{t;i,j+\frac{1}{2}}-1, \tag{23}$$

$$E_i=-\frac{\phi_{i+1}-\phi_{i-1}}{2\Delta x}. \tag{24}$$

It is noted that the numerical integration in the right hand side of Eq. (23) is performed by using the line-integrated values. This calculation is more rigorous compared with the other numerical integrations such as trapezoid and Simpson ones. It is possible to apply more accurate Poisson solver such as the fourth-order discretization by introducing the line-integrated scalar potential and the Fourier solver to the left hand side of Eq. (23). However, we have only used the conventional second-order central FDM for the Poisson equation in this paper, since there is no qualitative change regardless of the Poisson solver in some numerical tests.

In the following, we show the case of $v_j < 0$ and $E_i > 0$. The interpolation functions for the upwind discretization of $f(x, v)$ along the x and v directions are constructed as

$$F(x; f_{i,j}, f_{i+1,j}, \rho_{i+\frac{1}{2}j}) = a(x - x_i)^2 + b(x - x_i) + c \tag{25}$$

with

$$\begin{cases} a = \dfrac{3(f_{i,j} + f_{i+1,j})}{\Delta x^2} - \dfrac{6\rho_{i+\frac{1}{2}j}}{\Delta x^3}, \\ b = -\dfrac{2(2f_{i,j} + f_{i+1,j})}{\Delta x} + \dfrac{6\rho_{i+\frac{1}{2}j}}{\Delta x^2}, \\ c = f_{i,j}, \end{cases} \tag{26}$$

and

$$G(v; f_{i,j}, f_{i,j+1}, \zeta_{ij+\frac{1}{2}}) = p(v - v_j)^2 + q(v - v_j) + r \tag{27}$$

with

$$\begin{cases} p = \dfrac{3(f_{i,j} + f_{i,j+1})}{\Delta v^2} - \dfrac{6\zeta_{ij+\frac{1}{2}}}{\Delta v^3}, \\ q = -\dfrac{2(2f_{i,j} + f_{i,j+1})}{\Delta v} + \dfrac{6\zeta_{i,j+\frac{1}{2}}}{\Delta v^2}, \\ r = f_{i,j}, \end{cases} \tag{28}$$

respectively. Then, $f_{x;i,j}$ and $f_{v;i,j}$ in Eq. (16) are determined by using these interpolation functions as

$$f_{x;i,j} = \left.\frac{\partial f}{\partial x}\right|_{(x,v)=(x_i,v_j)} \simeq \frac{\partial}{\partial x} F(x; f_{i,j}, f_{i+1,j}, \rho_{i+\frac{1}{2}j})|_{x=x_i}, \tag{29}$$

$$f_{v;i,j} = \left.\frac{\partial f}{\partial v}\right|_{(x,v)=(x_i,v_j)} \simeq \frac{\partial}{\partial v} G(v; f_{i,j}, f_{i,j+1}, \zeta_{ij+\frac{1}{2}})|_{v=v_j}. \tag{30}$$

Here, we introduce two numerical methods for performing the integration in Eqs. (17)–(19). One is a simplified version that replaces the velocity and electric field in the integrand with the average ones as follows:

$$\int_{v_j}^{v_{j+1}} v f_x(x_i, v) dv \simeq \bar{v} \int_{v_j}^{v_{j+1}} f_x(x_i, v) dv = \bar{v} \zeta_{x;i,j+\frac{1}{2}}, \tag{31}$$

$$\int_{x_i}^{x_{i+1}} E(x) f_v(x, v_j) dx \simeq \bar{E} \int_{x_i}^{x_{i+1}} f_v(x, v_j) dx = \bar{E} \rho_{v;i+\frac{1}{2}j}, \tag{32}$$

where $\bar{v}$ and $\bar{E}$ denote the averaged velocity and electric field between grids as

$$\bar{v} \equiv \int_{v_j}^{v_{j+1}} v\, dv / \Delta v = \frac{v_j + v_{j+1}}{2}, \tag{33}$$

$$\bar{E} \equiv \int_{x_i}^{x_{i+1}} E(x) dx / \Delta x = -\frac{\phi_{i+1} - \phi_i}{\Delta x}. \tag{34}$$

The other is a more strict version that replaces the distribution functions in the integrand with the interpolated ones as follows:

$$\int_{v_j}^{v_{j+1}} v f_x(x_i, v) dv = \int_{v_j}^{v_{j+1}} v G(v; f_{x;i,j}, f_{x;i,j+1}, \zeta_{x;i,j+\frac{1}{2}}) dv, \tag{35}$$

$$\int_{x_i}^{x_{i+1}} E(x) f_v(x, v_j) dx = \int_{x_i}^{x_{i+1}} E(x) F(x; f_{v;i,j}, f_{v;i+1,j}, \rho_{v;i+\frac{1}{2}j}) dx. \tag{36}$$

Here, $\zeta_{x;i,j+\frac{1}{2}}$ in Eqs. (31) and (35) and $\rho_{v;i+\frac{1}{2}j}$ in Eqs. (32) and (36) are calculated through

$$\zeta_{x;i,j+\frac{1}{2}} = \frac{\partial}{\partial x} F(x; \zeta_{i,j+\frac{1}{2}}, \zeta_{i+1,j+\frac{1}{2}}, M_{i+\frac{1}{2}j+\frac{1}{2}})|_{x=x_i}, \tag{37}$$

$$\rho_{v;i+\frac{1}{2}j} = \frac{\partial}{\partial v} G(v; \rho_{i+\frac{1}{2}j}, \rho_{i+\frac{1}{2}j+1}, M_{i+\frac{1}{2}j+\frac{1}{2}})|_{v=v_j}, \tag{38}$$

respectively. $E(x)$ in Eq. (36) is determined by using third-order central interpolation. In this paper, we refer to the former scheme as the IDO-CF1, and the latter one as the IDO-CF2. Note that both schemes conserve the total particle number:

$$N \equiv \sum_{i=1}^{N_x} \sum_{j=1}^{N_v} M_{i+\frac{1}{2}j+\frac{1}{2}} \tag{39}$$

by using Eq. (19).

3. Numerical simulations of the Vlasov–Poisson equation system

In this section, we applied the IDO-CF scheme to two-dimensional Vlasov simulation of the nonlinear Landau damping (Section 3.1) and two-stream instability (Section 3.2). We focused on studying the accuracy and efficiency of the scheme by comparing it with other numerical schemes such as the Spline and CIP ones. Besides the L1-norm and energy conservation, we investigated the conservation property of the entropy and phase space area occupied by the distribution function, which are related to Liouville's theorem and are important measures in identifying the complex dynamics in phase space.

3.1. Nonlinear Landau damping

First, we investigated the nonlinear Landau damping (NLD) with the initial condition:

$$f(t=0,x,v)=\frac{1}{\sqrt{2\pi}}\exp\left(-\frac{v^2}{2}\right)\left(1+B\cos\frac{2\pi}{L_x}x\right), \tag{40}$$

where $L_x=4\pi,\ V_{max}=10,\ (N_x,N_v)=(64,1023),\ \Delta t=5\times10^{-2}$ and the perturbation amplitude $B=0.5$ were chosen as a typical case. In this paper, we use the fourth-order Runge–Kutta scheme in the time integration, since higher-order Runge–Kutta scheme can enlarge Courant number limitation [20] whereas the contribution to the numerical accuracy is small. This has been studied in numerous reports in the literature [11,15,16,21–23,27] as a fundamental test of the collisionless Landau damping and subsequent nonlinear evolution of the electrostatic field dominated by wave–particle interaction. The time history of the field energy for the IDO-CF2 scheme is shown in Fig. 1(a1) and (a2), where (a1) is the evolution of a short time scale ($0<t<200$), and (a2) a longer time scale ($0<t<1000$). The short time scale evolution is in good agreement with the results given in the literature, i.e., the exponential damping of initial electrostatic field perturbation, subsequent growth and saturation due to particle trapping, and bounce motion in phase space. The real frequency and phase velocity of the plasma wave, which are given as $\omega\simeq1.42$ and $v_{ph}=\omega/k\simeq2.8$, agree with those obtained from the dispersion relation.

The distribution functions in phase space are shown in Fig. 2, which are plotted using a linear scale at six different stages. The distribution functions using a logarithmic scale are also shown in Fig. 3, where the region of $f\geqslant f_{min}=10^{-2}$ is shaded. Hereafter, we regard the shaded region as an approximate phase space area occupied by the distribution function

$$A(t)\equiv\int\int_{f\geqslant f_{min}}dx\,dv. \tag{41}$$

Note that the phase space area is conserved, i.e., $dA/dt=0$, as far as the system follows the Hamiltonian dynamics and/or equivalently Liouville's theorem. During the initial damping phase of the electrostatic field ($0<t<20$), ballistic modes which cause tilted zonal structure are found to be excited, as seen in Fig. 2(b) and (c). This structure results from the particle acceleration due to the initially applied strong electrostatic field. Then, the distribution becomes unstable to plasma wave so that the field energy grows and then saturates due to the particle trapping ($20<t<40$), as shown in Figs. 1(a) and 2(d). After the saturation, bounce motion along the separatrix causes amplitude oscillation as seen in Figs. 1(a) and 2(d)–(e). The period of the bounce motion at the quasi-steady state is estimated as $T_b\sim40$ from Fig. 1(a), which is approximately the same as the theoretical one $T_b\simeq2\pi\sqrt{m/eE_0k}\sim41.9$. Here, we have employed $k=0.5$ and $E_0\sim0.045$. It was observed that the zonal structure due to the ballistic mode becomes finer with time and ultimately disappears, as seen in Fig. 2(f).

Next, we investigated the time histories of the kinetic energy, field energy and also total energy $E(t)$ for the IDO-CF2 scheme in Fig. 4(a) and those of $\Delta\epsilon\equiv[E(t)-E(0)]/E(0)$ for four different schemes in Fig. 4(b) in an initial time interval ($0<t<30$). Note that the constraint for the total particle number is imposed in the present four schemes, namely $\sum_{i=1}^{N_x}\sum_{j=1}^{N_v}f_{i,j}\Delta x\Delta v$ is kept constant for the Spline/CIP schemes and N defined by Eq. (39) for the IDO-CF1/IDO-CF2 ones, so that the energy conservation is relatively high for all four schemes with no secular increase after $t\sim5$. On the other hand, the total energy error of the IDO-NCF scheme (not shown in Fig. 1) does not saturate, but slightly increases. This originates from that the mass conservation is not ensured for the IDO-NCF scheme. The IDO-CF2 scheme shows a higher accuracy than the Spline, CIP and IDO-CF1 schemes in the initial phase ($0<t<5$), where the initially applied large amplitude wave causes a strong particle acceleration. This results from the fact that the constraint for the IDO-CF scheme corresponds to rigorous particle conservation, whereas that of the Spline/CIP scheme is an approximate one, which is equivalent to rectangular integration.

The time history of the variation of the discretized L1-norm defined by $\Delta m\equiv[M(t)-M(0)]/M(0)$ is shown in Fig. 1(b), where $M(t)=\sum_{i=1}^{N_x}\sum_{j=1}^{N_v}|f_{i,j}|$. Note that Δm represents the ratio of the negative value of the distribution function to the whole one since the total particle number is conserved for all schemes. The L1-norm in the Spline scheme increases from early nonlinear phase around $t\sim15$. This is due to the fact that the Spline scheme exhibits numerical oscillation for short wavelength components. However, the numerical oscillation tends to be diminished due to numerical diffusion, and then the L1-norm comes back to the initial value after several bounce periods. Note that the relative error of the L1-norm is about 6.63×10^{-5} at $t=1000$. On the other hand, although multi-moment schemes such as the CIP, IDO-CF1 and IDO-CF2 ones also show the increase of the L1-norm, the ratio is small, as seen in Fig. 1(b). This demonstrates an advantage of the multi-moment schemes in reducing numerical oscillation and maintaining stability for a long time scale Vlasov simulation.

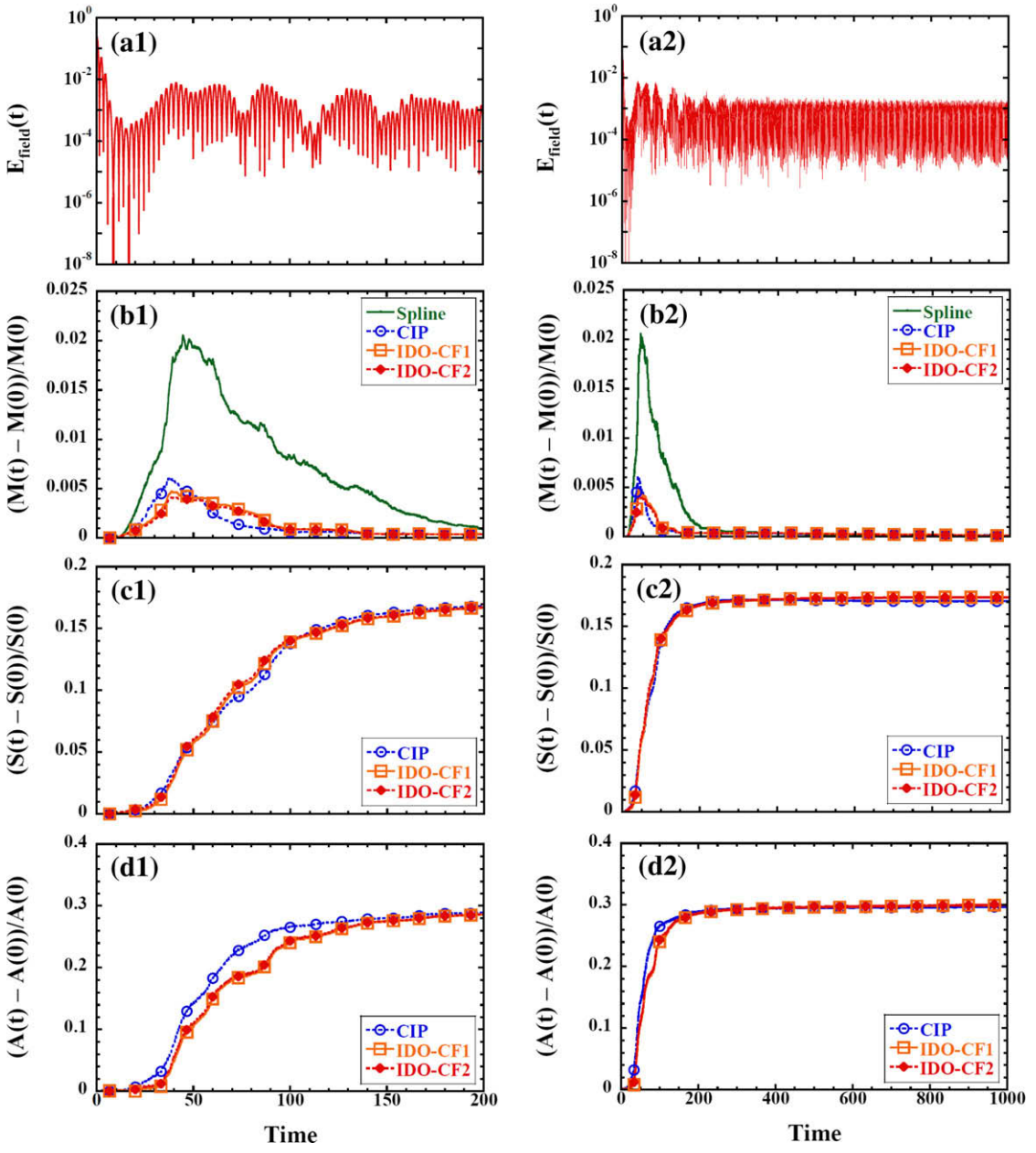

Fig. 1. Time evolution of field energy for the IDO-CF2 scheme in (a1) a short time scale ($0 \leqslant t \leqslant 200$) and (a2) a long time one ($0 \leqslant t \leqslant 1000$). Time evolutions of the deviation from the initial values of (b) L1-norm, (c) entropy and (d) phase space area for different numerical schemes (Spline, CIP, IDO-CF-1 and IDO-CF-2). Both the short time scale ($0 \leqslant t \leqslant 200$) ((b1), (c1) and (d1)) and long time scale ($0 \leqslant t \leqslant 1000$) ((b2), (c2) and (d2)) are illustrated.

Next, we investigate the entropy S defined by

$$S(t) \equiv \int\int f(t,x,v)\ln f(t,x,v)dx\,dv \tag{42}$$

and also the phase space area A defined by Eq. (41). The entropy is conserved, i.e., $dS/dt = 0$, for the Hamiltonian dynamics system. Fig. 1(c) and (d) shows the time history of $\Delta s \equiv \{S(t) - S(0)\}/S(0)$ and $\Delta a \equiv \{A(t) - A(0)\}/A(0)$, respectively. It was found that Δs and Δa exhibit a similar tendency as they are kept constant up to around $t \sim 15$, where the field energy damps down to the minimum level, but starts to increase (or deviate) just after the field energy exponentially grows due to the onset of the instability (see Fig. 1(a)). They keep increasing, and then saturate at around $t \sim 150$. The time interval causing saturation roughly corresponds to the four bounce periods from the onset of the instability. These results show that the entropy and phase space area are linked to each other. Note that the total energies are almost kept constant for all three schemes.

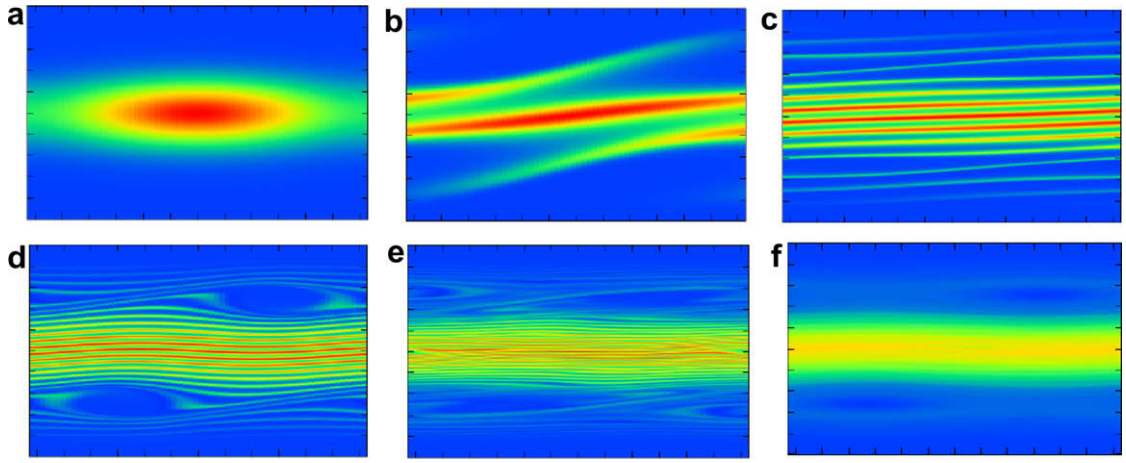

Fig. 2. Contour plots of the distribution function (linear plot) in phase space at six different snap times: (a) $t = 0$, (b) $t = 5$, (c) $t = 20$, (d) $t = 40$, (e) $t = 80$ and (f) $t = 1000$, for the IDO-CF2 scheme. The domain $R = \{(x, v) \,|\, |x| \leqslant 2\pi, |v| \leqslant 5\}$ is illustrated.

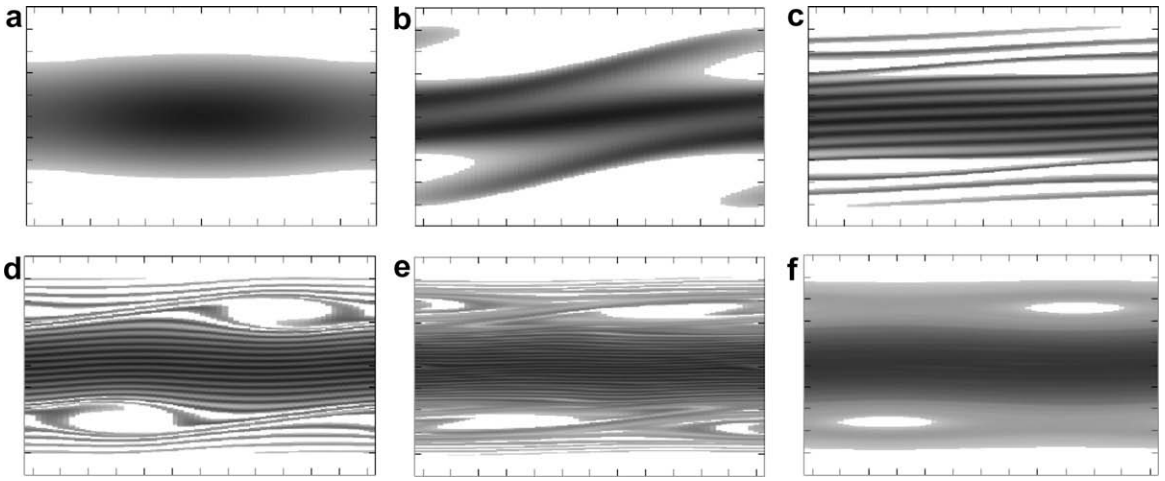

Fig. 3. Contour plots of the distribution function (logarithmic plot) in phase space at six different snap times: (a) $t = 0$, (b) $t = 5$, (c) $t = 20$, (d) $t = 40$, (e) $t = 80$ and (f) $t = 1000$, for the IDO-CF2 scheme. The region of $f \geqslant f_{min} = 10^{-2}$ is shaded. The domain $R = \{(x, v) \,|\, |x| \leqslant 2\pi, |v| \leqslant 5\}$ is illustrated.

Here, we discuss the deviation from Liouville's theorem in these numerical simulations. Note that the typical time scale of aliasing error due to the ballistic mode excitation is estimated as $t_{alias} = 1/k\Delta v \sim 102$ using $\Delta v = 20/1023$ and $k = 0.5$, which is much longer than the time when S and A start to increase ($t \sim 20$). Therefore, it can be seen that the deviation originates from the particle trapping due to the finite amplitude wave and subsequent bounce motion along the separatix. Namely, strong distortion of the distribution function takes place near the separatrix due to the singularity of the particle dynamics such that the particles with $H > H_0$ follows the passing orbit, whereas that with $H < H_0$ is trapped, where H_0 denotes the energy of the particle on the separatrix. Then, a small element of the distribution function on the separatrix is severely stretched, leading to a complicated folded structure, so that infinitesimally small numerical perturbations cause ergotization. This is also illustrated by Fig. 5 where the time evolution of the entropy in Fig. 1(c) is investigated by dividing the entropy into two regions, i.e., $|v| < 1$ and $|v| > 1$. It can be clearly seen that the increase of entropy observed in Fig. 1(c) dominantly originates from the region of $|v| > 1$ where the separatrix and the trapping region exist. Meanwhile, the slight increase of the entropy is observed in the region of $|v| < 1$ at around $t \sim 70$. This may come from the numerical error for the interpolation when the wavelength of the ballistic mode to the v-direction becomes $\lambda_b = 3\Delta v/2$. However, the rate of the entropy increase in $|v| < 1$ is small ($\sim 20\%$) compared with that of the total amount. Therefore, it can be seen that the deviation from Liouville's theorem is mainly caused by the ergotization near the separatrix.

Here, we investigate the time history of $\Delta\epsilon$ and Δs by changing the resolution in phase space in Figs. 6 and 7, where the number of mesh points in configuration space N_x is changed in Fig. 6 and that in velocity space N_v in Fig. 7. As the resolution is increased both in configuration and velocity space, the typical time scale in which S begins to increase and also saturates is

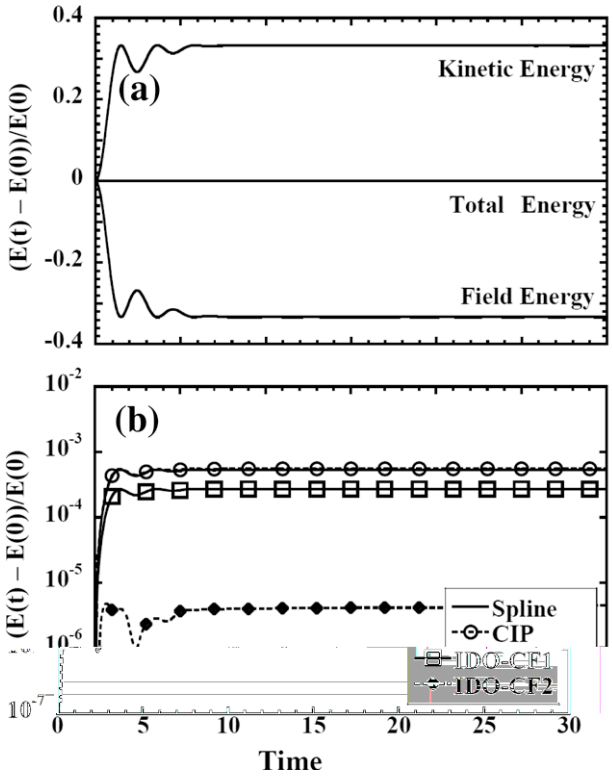

Fig. 4. (a) Time evolutions of the field energy, kinetic energy and total energy for the IDO-CF2 scheme in $0 \leqslant t \leqslant 30$. (b) Time evolution of the relative total energy error in the early time for different numerical schemes in $0 \leqslant t \leqslant 30$.

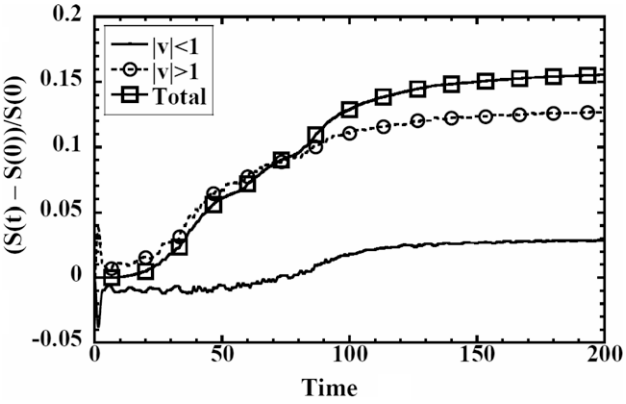

Fig. 5. Time evolutions of the entropy in the region of $|v| < 1$ and that of $|v| > 1$. The total one is also shown.

delayed, whereas S reaches an asymptotic value. On the other hand, the energy conservation depends on N_x since it is influenced by the Poisson equation.

Finally, we discuss the computational cost of each scheme. The ratio of the total time of computation for the NLD tests up to $t = 1000$ is given as CIP:Spline:IDO-CF1(4th RK):IDO-CF2(4th RK) = 1:1.73:3.08:4.59. It is found that the IDO-CF scheme has higher costs. Therefore, it may be useful to introduce the lower Runge–Kutta scheme for reducing the computational costs. The total time of computation for IDO-CF scheme is almost proportional to the order of Runge–Kutta scheme as IDO-CF2(2nd RK):IDO-CF2(3rd RK):IDO-CF2(4th RK) = 1:1.44:1.92.

3.2. Two-stream instability

Here, we investigated the two-stream instability (TSI) using the same four numerical schemes as were used in Section 3.1 with the initial condition:

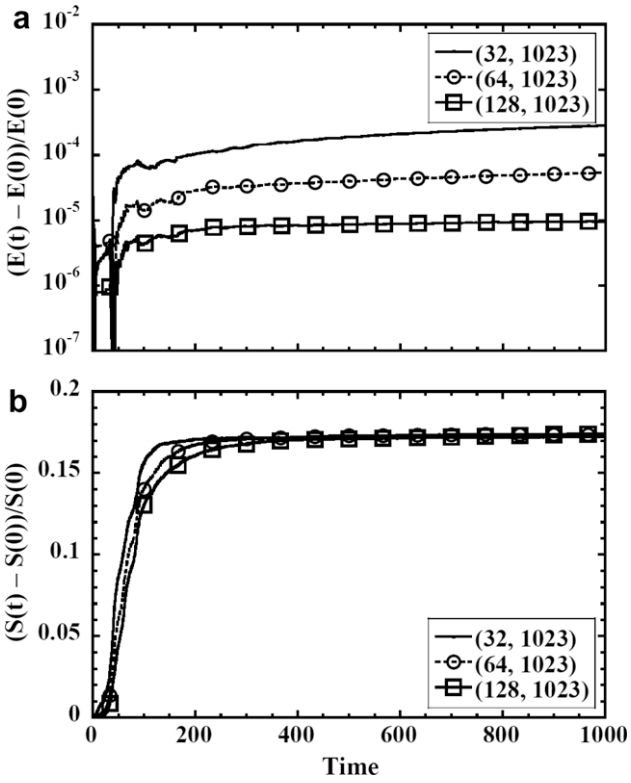

Fig. 6. Time evolutions of (a) the relative total energy error and (b) the deviation from the initial values of the entropy for different number of mesh points to the x-direction.

$$f(t=0,x,v)=\frac{1}{\sqrt{2\pi}}v^2\exp\left(-\frac{v^2}{2}\right)\left(1+B\cos\frac{2\pi}{L_x}x\right), \tag{43}$$

where $B=10^{-5}$, $V_{max}=10$, $(N_x,N_v)=(128,511)$ and $\Delta t=10^{-3}$ are chosen as typical parameters. In Section 3.2.1, we study the case of $L_x=4\pi$, i.e., the corresponding minimum wave number $k_x=0.5$ which locates around the maximum growth rate. Therefore, in this case, only a single vortex survived in the system. Then, we extend the computational domain to $L_x=20\pi$ in Section 3.2.2 to investigate the coalescence process of vortices.

3.2.1. Single vortex dynamics

The time history of the field energy by using the IDO-CF2 scheme is shown in Fig. 8(a). After the linear growth and subsequent saturation, the field energy exhibits amplitude oscillation, whereas it converges to a constant value. The distribution functions in phase space are shown in Fig. 9 with a linear scale and in Fig. 10 with a logarithmic one. In Fig. 10, the region of $f\geqslant f_{min}=10^{-2}$ is shaded as in Fig. 3. After the saturation, trapping that causes a fine scale structure near the separatrix takes place, but it also disappears during about four bounce periods as in the NLD case, leading to a coarse-grained distribution.

The total energy conservation is well satisfied as shown in Fig. 11(a). A more detailed investigation shows that the energy is conserved in the linear and saturation phase ($0\leqslant t\leqslant 50$) in the IDO-CF2 scheme as shown in Fig. 11(b), whereas other schemes exhibit an error in the order of 10^{-5} from $t\sim 40$. Thus, the IDO-CF2 scheme shows excellent energy conservation due to the same reason as is explained in the NLD case.

The time history of the variation of the L1-norm in Fig. 8(b) also shows the same tendency as the time history in the NLD case. Namely, the L1-norm in the Spline scheme increases in the nonlinear phase ($t\geqslant 50$), and then slowly falls to zero. However, the increase is much smaller than that in the NLD case. This is due to the fact that the complex trapping dynamics takes place around $v_{ph}=0$ in the TSI case, whereas they occur around $v_{ph}\sim 2.8$ in the NLD case where the distribution is relatively small.

Next, we investigated the entropy S (Eq. (42)) and phase space area A (Eq. (41)) in Fig. 8(c) and (d), respectively. Note that A is also defined as the region of $f\geqslant f_{min}=10^{-2}$ same as in Fig. 10. The evolutions of S and A show similar tendency as those in Fig. 1(c) and (d), but the variations of S and A are the order of 2, which are small compared with those in Fig. 1(c) and (d).

We also investigated the energy E and entropy S for different resolutions in Figs. 12 and 13. As seen in Figs. 12 and 13(a), $\Delta\epsilon$ linearly increases after the saturation ($t\sim 100$). However, the total energy conservation is improved with N_x, suggesting that the numerical error originates from the Poisson equation (Eq. (23)). On the other hand, Δs depends on N_x and N_v.

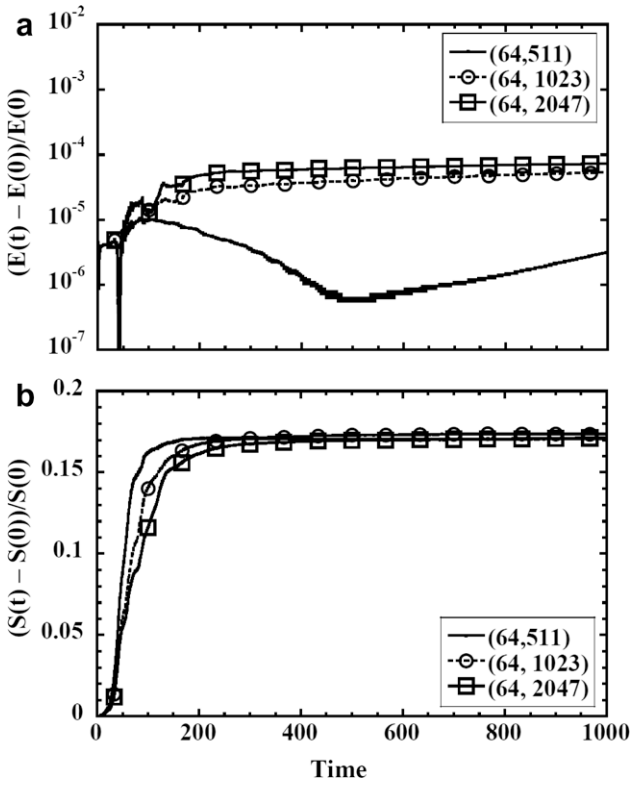

Fig. 7. Time evolutions of (a) the relative total energy error and (b) the deviation from the initial values of the entropy for different number of mesh points to the v-direction.

3.2.2. Multi-vortex dynamics and coalescence process

Next we investigated the TSI under the system size $L_x = 20\pi$ with the following two initial conditions:

$$f(t=0,x,v) = f_0(v)\left(1 + B\sum_{n=1}^{n_{max}} \cos\frac{2\pi}{L_x}nx\right), \tag{44}$$

$$f(t=0,x,v) = f_0(v)\left\{1 + B\sum_{n=1}^{n_{max}} \cos\left(\frac{2\pi}{L_x}nx + \phi_n\right)\right\}, \tag{45}$$

where $f_0(v) = 1/\sqrt{2\pi}v^2\exp(-v^2/2)$. Here, ϕ_n represents the phase factor for the initial perturbation which is randomly chosen between $[0, 2\pi]$. In the following, we refer to the above two cases as case-1 (Eq. (44)) and case-2 (Eq. (45)), for which the initial density perturbations defined as $\delta n(x, t=0) = \int(f(x,v,t=0) - f_0(v))dv$ are shown in Fig. 14. Namely, a single localized perturbation is set at $x = 0$ in case-1, whereas a random distribution constructed by the phase factors $\{\phi_n\}$ is set in case-2. Note that the perturbation in case-1 is an even function with respect to $x = 0$, so that excited waves due to the TSI should keep point symmetry to the origin, i.e., $(x, v) = (0, 0)$ in phase space. Fig. 15 shows the time evolution of the entropy in each case using the IDO-CF2 scheme. The contour plots of the distribution function for case-1 and case-2 are shown in Figs. 16 and 19 at six different stages, respectively.

In case-1, the mode $n = 3$, which roughly corresponds to that of the maximum linear growth rate, becomes dominant so that three vortices are initially established in phase space (Fig. 16(a)). Note that a symmetric structure with respect to the origin was confirmed, as was expected. Then, two vortices located at both sides of the origin start to merge together (Fig. 16(b)), leading to a state consisting of two vortices with different scales (Fig. 16(c)). Through this process, the fine scale structure associated with the topological change of the distribution is manifested. However, this structure disappears with time, indicating that the distribution is coarse-grained (Fig. 16(d)). In this phase, the entropy also increases, as seen in Fig. 15(a), due to the same reasons as discussed in Section 3.1. However, it is noted that such a complex merging and coarse-grained process evolve, keeping a symmetric structure with respect to the origin.

It is interesting to investigate such a merging process in wave number space, as is illustrated in Fig. 17. In the early phase before merging takes place, the spectra with lower mode numbers ($n \leqslant 10$) dominate (Fig. 17(a)), whereas higher ones increase as the merging evolves (Fig. 17(b)). After the fine scale structure becomes coarse-grained, the spectra with higher components are also reduced (Fig. 17(c)). Note that the spectra dominantly consist of even harmonics with a cosine function

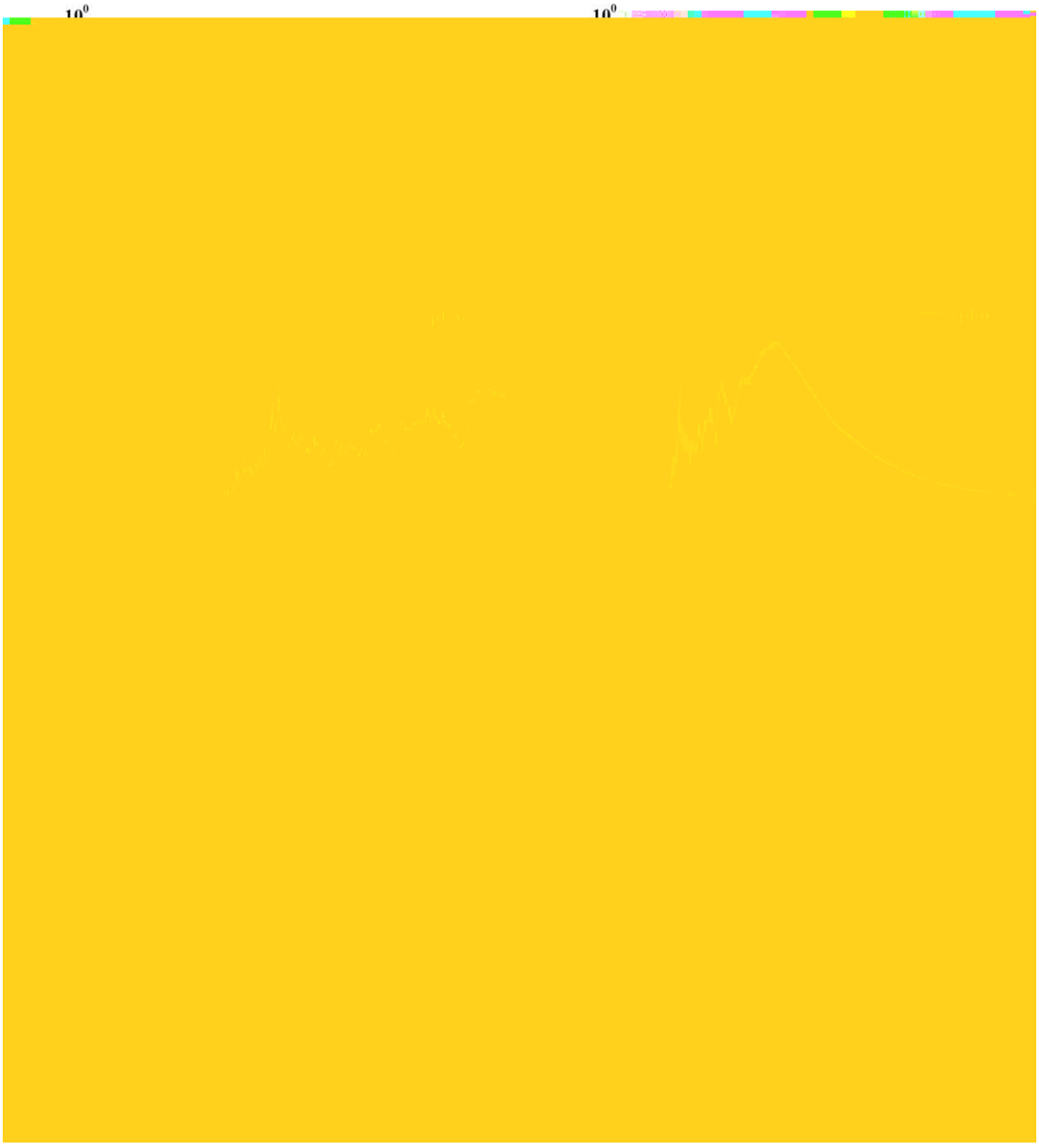

Fig. 8. Time evolution of field energy for the IDO-CF2 scheme in (a1) a short time scale ($0 \leqslant t \leqslant 200$) and (a2) a long time one ($0 \leqslant t \leqslant 1000$). Time evolutions of the deviation from the initial values of (b) L1-norm, (c) entropy and (d) phase space area for different numerical schemes (Spline, CIP, IDO-CF-1 and IDO-CF-2). Both the short time scale ($0 \leqslant t \leqslant 200$) ((b1), (c1) and (d1)) and long time scale ($0 \leqslant t \leqslant 1000$) ((b2), (c2) and (d2)) are illustrated.

shown by the red line in Fig. 17, due to the symmetric nature of the distribution. The system with two vortices (Fig. 16(d)) persists for a long time, keeping the entropy almost constant (see $200 \leqslant t \leqslant 4200$ in Fig. 15(b)), suggesting that the system satisfies a quasi-stable symmetric BGK equilibrium same as the one in the Bump-On-Tail instability. However, the odd harmonics shown by the blue line in Fig. 17 were found to appear gradually. Then the symmetry of the system breaks up and two vortices merge together at around $t = 4300$, leading to a single large scale vortex, as seen in Fig. 16(e) and (f). Such symmetry breaking is found to originate from the excitation of odd harmonic components, as seen in Fig. 17(d)–(f).

In order to present the physical reason for the symmetry breaking, we show the time evolution of the electrostatic fields by dividing the fields into even and odd harmonics in Fig. 18. At first, the even components grow linearly by exhausting the free energy of counter streaming, and then saturate at around $t \sim 40$. In this phase, the odd components are almost zero due

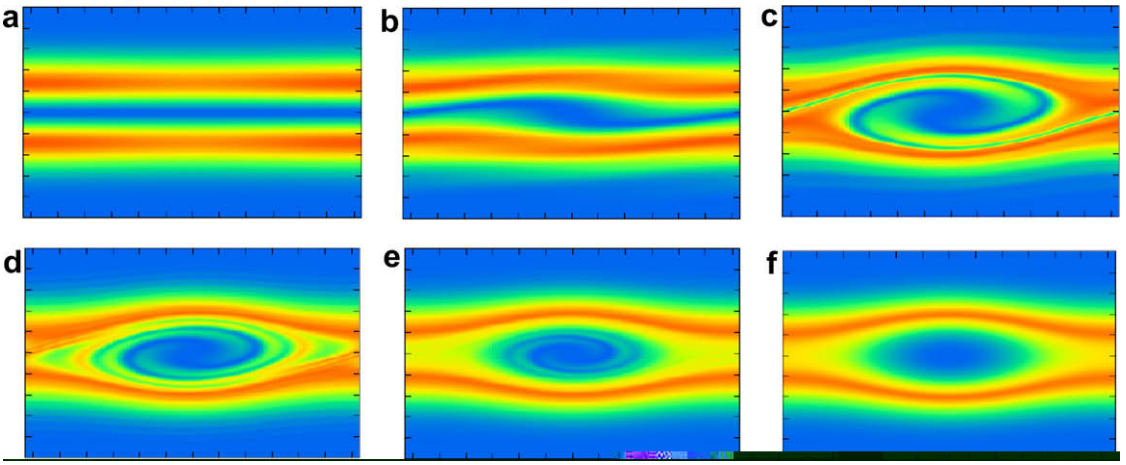

Fig. 9. Contour plots of the distribution function (linear plot) in phase space at six different snap times: (a) $t = 0$, (b) $t = 10$, (c) $t = 20$, (d) $t = 40$, (e) $t = 80$ and (f) $t = 1000$, for the IDO-CF2 scheme. The domain $R = \{(x, v) \,|\, |x| \leqslant 2\pi, |v| \leqslant 5\}$ is illustrated.

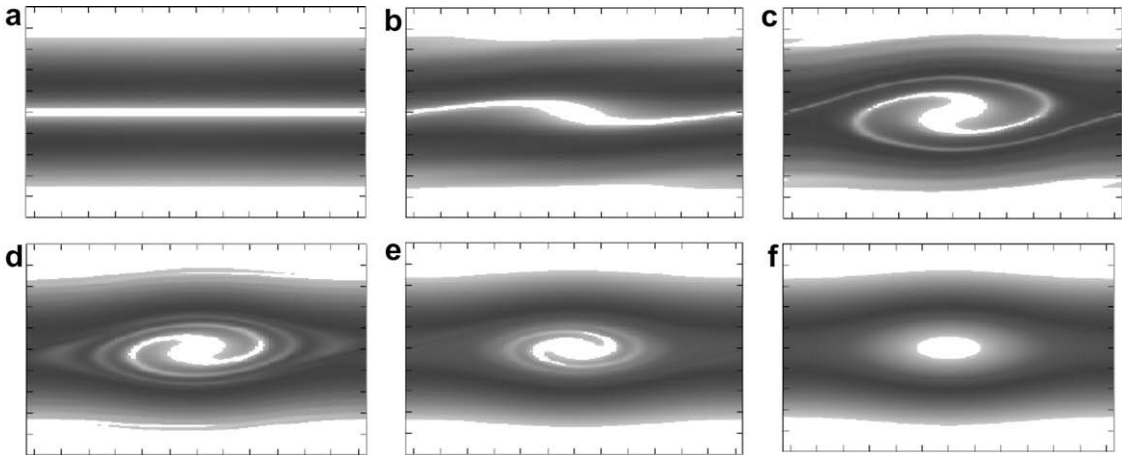

Fig. 10. Contour plots of the distribution function (logarithmic plot) in phase space at six different snap times: (a) $t = 0$, (b) $t = 10$, (c) $t = 20$, (d) $t = 40$, (e) $t = 80$ and (f) $t = 1000$, for the IDO-CF2 scheme. The region od $f \geqslant f_{min} = 10^{-2}$ is shaded. The domain $R = \{(x, v) \,|\, |x| \leqslant 2\pi, |v| \leqslant 5\}$ is illustrated.

to the initial condition, but start to increase to the level 10^{-8} in accordance with the saturation of even harmonics. This phase is also coincident with that of entropy increase (Fig. 18(a)), suggesting that the ergotization process of the fine scale structure also causes a numerical noise with a small level. Then, the odd harmonics start to grow linearly with a much smaller growth rate ($\gamma_{odd} = 1/40\gamma_{even}$) and reach to the same level as the even components, as seen in Figs. 17(e) and 18(b). This result indicates that the quasi-stable BGK equilibrium seen in Fig. 16(c) and (d) is unstable for the perturbation of odd harmonics, so that the small numerical noise becomes the seed of the instability, which causes a global change and/or symmetry breaking of the distribution function. However, the dynamics after the initial setting of the noise, i.e., exponential growth, saturation, coalescence, and the coarse-grained process, are considered to be deterministic without regard to the scheme.

In case-2, where the initial distribution is randomly set, the dynamics are qualitatively different. The most unstable mode $n = 4$ and subsequent four vortices are excited in the early stage (Fig. 19(a)). Then, the merging from four vortices to two takes place at first (Fig. 19(b) and (c)). Consequently, entropy increases to the same level as that in case-1 where three vortices are merged to two ($t \sim 180$), as seen in Fig. 15(a). Meanwhile, it was found that both even and odd components jointly evolve and remain at almost the same level, as seen in Fig. 20. Then, the merging from two to one is successively triggered (Fig. 19(d) and (e)), and the entropy increases again to the same level as that in case-1 where the two vortices are also merged to one, as seen in Fig. 15(b). It is interesting to note that we finally have a similar state with a single vortex in both case-1 and case-2 [27]. This state may correspond to a stable BGK solution, where the spectra of even and odd harmonics exhibit a similar distribution.

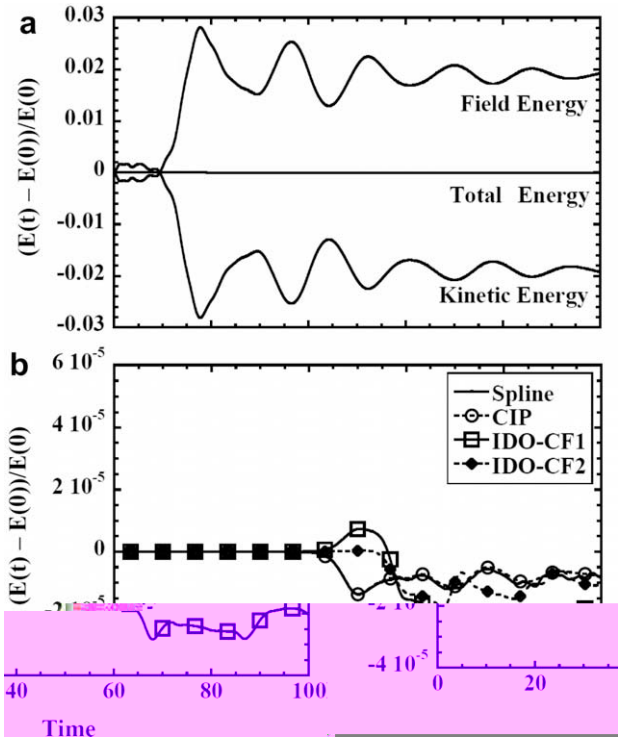

Fig. 11. Time evolutions of the field energy, kinetic energy and total energy for the IDO-CF2 scheme in $0 \leqslant t \leqslant 100$. (b) Time evolution of the relative total energy error in the early time for different numerical schemes in $0 \leqslant t \leqslant 100$.

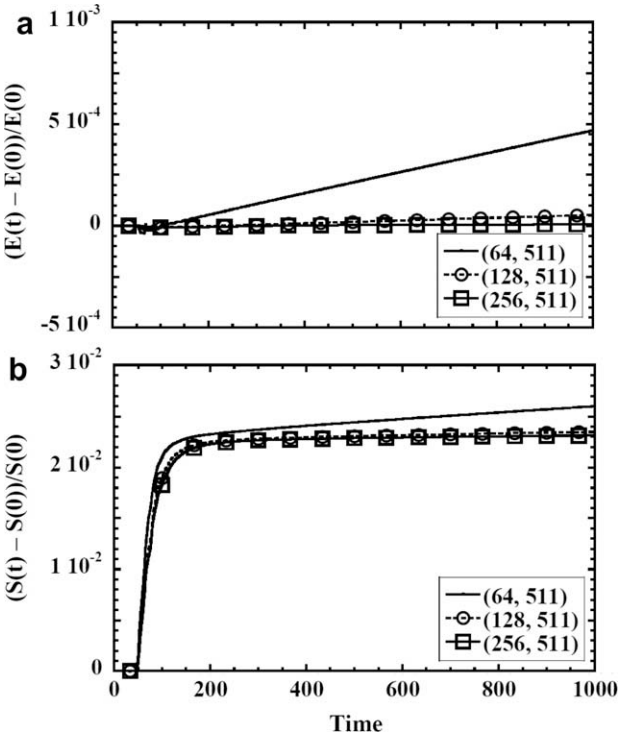

Fig. 12. Time evolutions of (a) the relative total energy error and (b) the deviation from the initial values of the entropy for different number of mesh points to the *x*-direction.

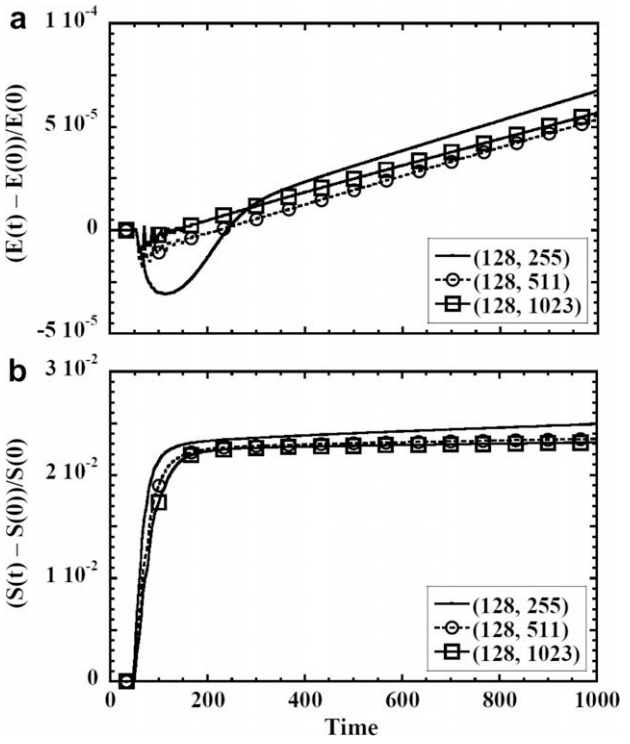

Fig. 13. Time evolutions of (a) the relative total energy error and (b) the deviation from the initial values of the entropy for different number of mesh points to the v-direction.

4. Application of the IDO-CF scheme to particular problems in plasmas

In this section, we applied the developed IDO-CF scheme to some particular problems which are important for the study of plasma physics, that is, phase space 2D Fokker–Planck simulation in Section 4.1, the phase space 4D Vlasov–Poisson simulation in Section 4.2 and the real space 2D guiding-center drift simulation in Section 4.3. Through these simulations, we showed that the IDO-CF scheme is efficient and superior in studying the phenomena in high dimensional system and also in the system with dissipation and drift motion.

4.1. Numerical simulations of the Fokker–Planck equation system

The IDO-CF2 scheme belongs to an Eulerian one and is thus easily extended to the Fokker–Planck simulation with the governing equation given by

$$\frac{\partial f(t,x,v)}{\partial t}+\frac{\partial\{vf(t,x,v)\}}{\partial x}-\frac{\partial\{E(t,x)f(t,x,v)\}}{\partial v}=\left\{\frac{\partial f(t,x,v)}{\partial t}\right\}_c, \tag{46}$$

which is coupled with the Poisson equation, Eq. (15). Here, $(\partial f/\partial t)_c$ represents the collision operator. Following reference [28], we have employed a simplified linear collision term given by

$$\left\{\frac{\partial f(t,x,v)}{\partial t}\right\}_c=\beta\left[D\frac{\partial^2 f(t,x,v)}{\partial v^2}+\frac{\partial\{vf(t,x,v)\}}{\partial v}\right], \tag{47}$$

where the effective collision frequency β is taken to be constant and the coefficient D is determined as

$$D=\int_{-\infty}^{\infty}\int_{-L_x/2}^{L_x/2}f(t,x,v)v^2\,dx\,dv\Big/\int_{-\infty}^{\infty}\int_{-L_x/2}^{L_x/2}f(t,x,v)dx\,dv \tag{48}$$

to ensure the energy conservation of the collision operator.

Now, we apply the central discretization to the collision operator. As discussed in Ref. [20], the central discretization can cause numerical oscillation in the calculation of advection terms, in particular with high wave number, so that the upwind discretization is employed in order to avoid such oscillations. On the other hand, there is no such a constraint for the collision

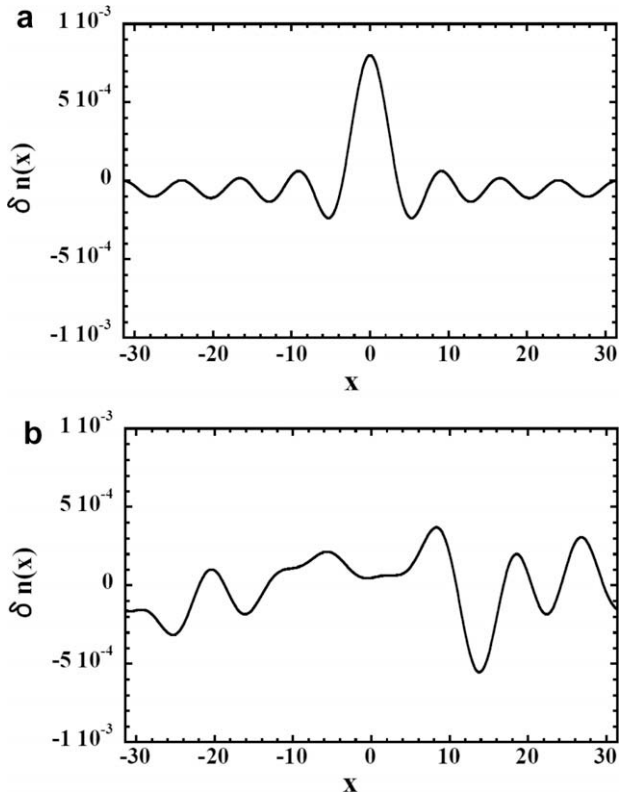

Fig. 14. Initial density perturbation consisting of (a) only even parity modes keeping symmetry with respect to $x = 0$ (case-1) and (b) randomly distributed even and odd modes (case-2).

terms, therefore we can utilize fourth-order central discretization. Here, we use the following fourth-order polynominal interpolation function along the v-direction as

$$G(v; f_{i,j-1}, f_{i,j}, f_{i,j+1}, \zeta_{i,j-\frac{1}{2}}, \zeta_{i,j+\frac{1}{2}}) = a(v - v_j)^4 + b(v - v_j)^3 + c(v - v_j)^2 + d(v - v_j) + e, \tag{49}$$

The five unknown coefficients in Eq. (49) can be determined by the five constraints,

$$G(v_{j-1}) = f_{i,j-1}, \tag{50}$$

$$G(v_j) = f_{i,j}, \tag{51}$$

$$G(v_{j+1}) = f_{i,j+1}, \tag{52}$$

$$\int_{v_{j-1}}^{v_j} G(v)dv = \zeta_{i,j-\frac{1}{2}}, \tag{53}$$

$$\int_{v_j}^{v_{j+1}} G(v)dv = \zeta_{i,j+\frac{1}{2}}, \tag{54}$$

as follows:

$$\begin{cases} a = \dfrac{5(f_{i,j-1} + 4f_{i,j} + f_{i,j+1})}{4\Delta v^4} - \dfrac{15(\zeta_{i,j+\frac{1}{2}} + \zeta_{i,j-\frac{1}{2}})}{4\Delta v^5}, \\ b = \dfrac{f_{i,j+1} - f_{i,j-1}}{\Delta v^3} - \dfrac{2(\zeta_{i,j+\frac{1}{2}} - \zeta_{i,j-\frac{1}{2}})}{\Delta v^4}, \\ c = -\dfrac{3(f_{i,j-1} + 8f_{i,j} + f_{i,j+1})}{4\Delta v^2} + \dfrac{15(\zeta_{i,j+\frac{1}{2}} + \zeta_{i,j-\frac{1}{2}})}{4\Delta v^3}, \\ d = -\dfrac{f_{i,j+1} - f_{i,j-1}}{2\Delta v} + \dfrac{2(\zeta_{i,j+\frac{1}{2}} - \zeta_{i,j-\frac{1}{2}})}{\Delta v^2}, \\ e = f_{i,j}. \end{cases} \tag{55}$$

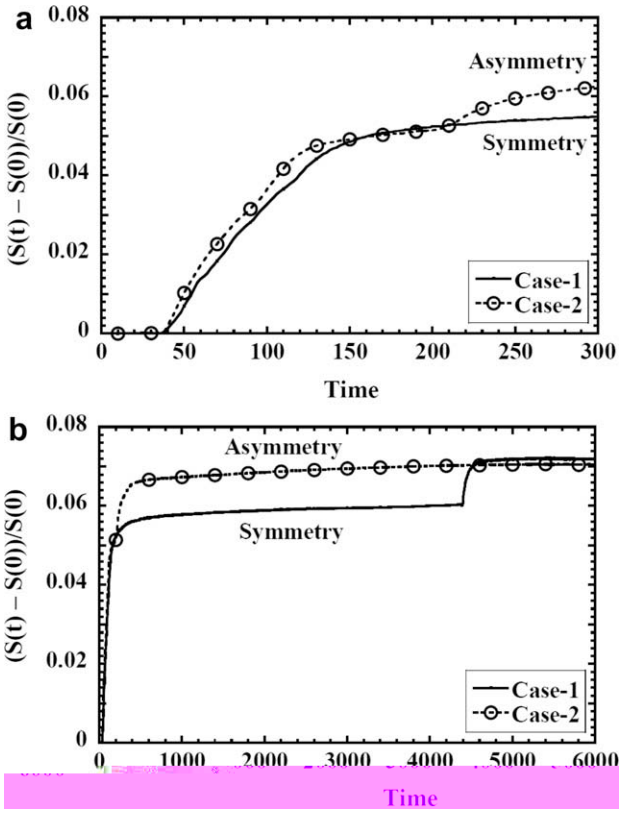

Fig. 15. Time evolutions of the deviation from the initial value of the entropy in case-1 and case-2. (a) Short time scale ($0 \leqslant t \leqslant 300$) and (b) long time scale ($0 \leqslant t \leqslant 6000$) are shown.

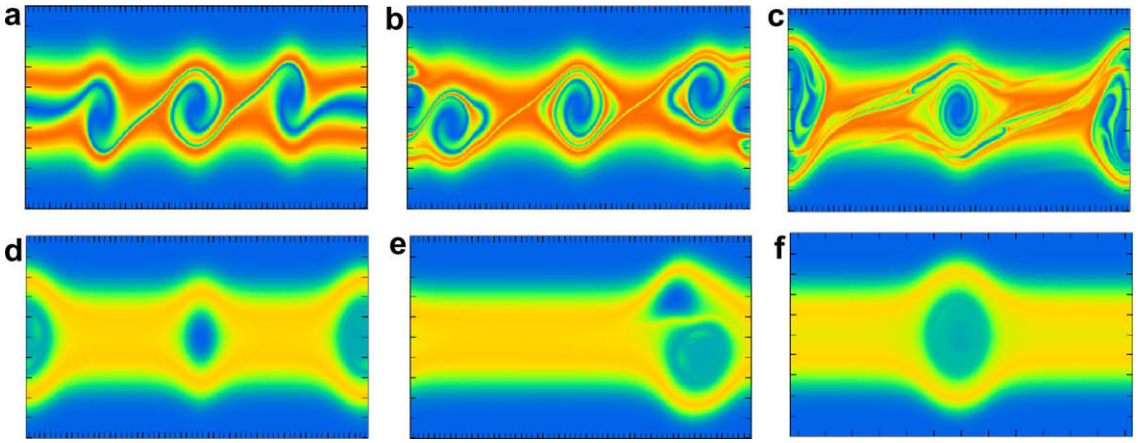

Fig. 16. Contour plots of the distribution function (linear plot) in phase space at six different snap times: (a) $t = 40$, (b) $t = 50$, (c) $t = 80$, (d) $t = 4000$, (e) $t = 4380$ and (f) $t = 6000$, in case-1. The domain $R = \{(x, v) \,|\, |x| \leqslant 10\pi, |v| \leqslant 5\}$ is illustrated.

Then, Eq. (47) is determined by using Eqs. (49) and (55) as

$$\left(\frac{\partial f}{\partial t}\right)_{c,ij} \simeq \beta\left[D\frac{\partial^2}{\partial v^2}G(v; f_{ij-1}, f_{ij}, f_{ij+1}, \zeta_{ij-\frac{1}{2}}, \zeta_{ij+\frac{1}{2}})|_{v=v_j} + \frac{\partial}{\partial v}\left\{vG(v; f_{ij-1}, f_{ij}, f_{ij+1}, \zeta_{ij-\frac{1}{2}}, \zeta_{ij+\frac{1}{2}})\right\}\Big|_{v=v_j}\right]. \tag{56}$$

We have applied the above scheme to the NLD case, as was done in Section 3.1. The time histories of (a) field energy, (b) L1-norm and (c1, c2) entropy are shown in Fig. 21 for $\beta = 0$, 10^{-5} and 10^{-4}, respectively. As the collision frequency β becomes large, the field energy decreases gradually and the amplitude oscillation becomes weak. In the case of $\beta = 10^{-4}$,

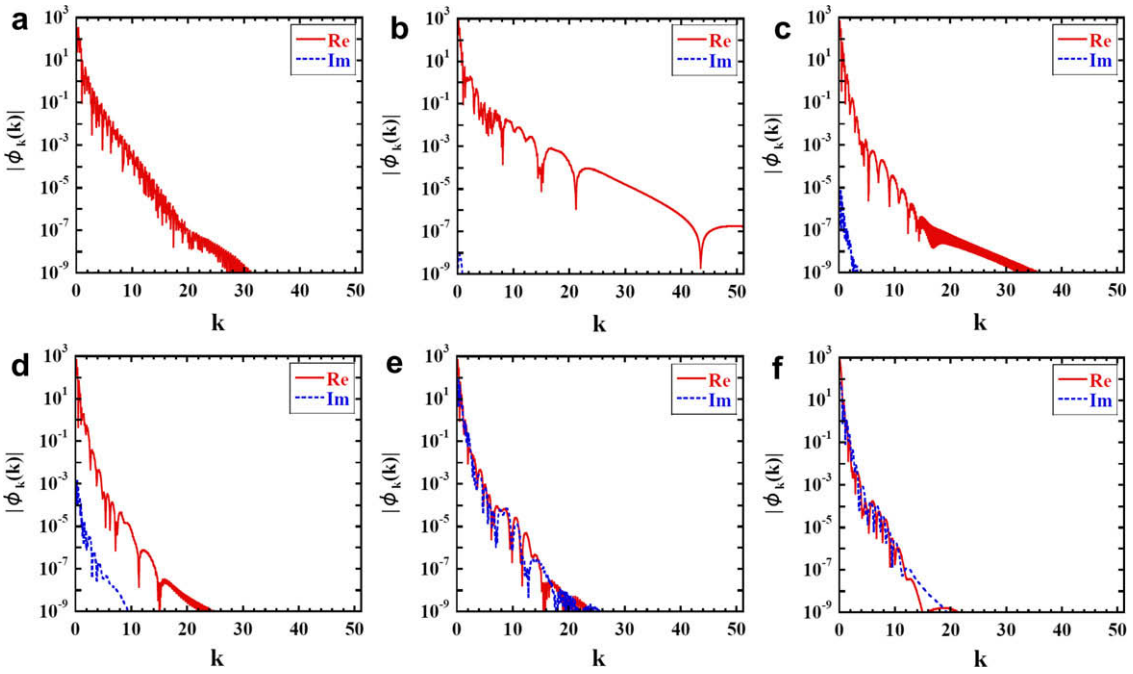

Fig. 17. Spectral distributions of the electrostatic potential $\phi(x)$ at six different snap times: (a) $t = 40$, (b) $t = 80$, (c) $t = 1000$, (d) $t = 2000$, (e) $t = 4000$ and (f) $t = 6000$, in case-1. A real part and imaginary part, which correspond to even and odd harmonics, respectively, are shown.

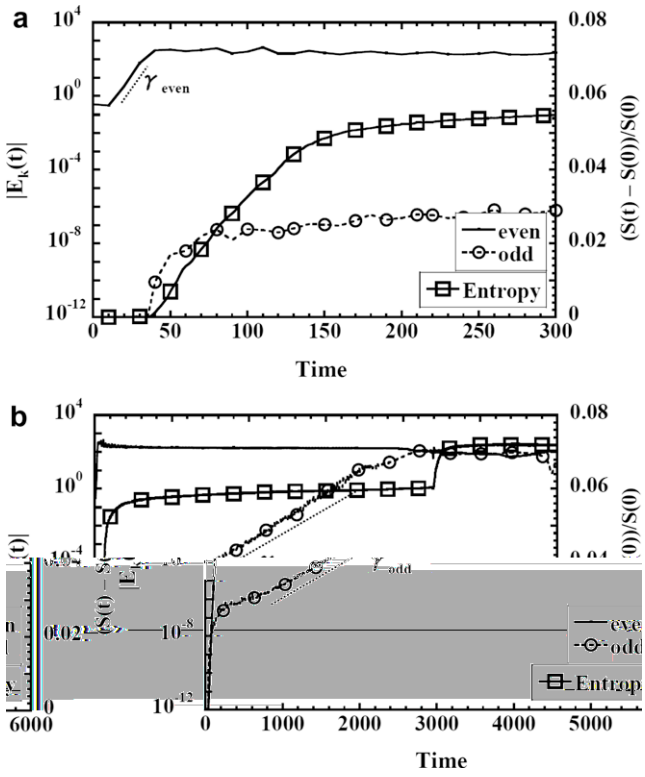

Fig. 18. Time evolutions of the electrostatic field divided into even and odd components in case-1. Both (a) a short time scale ($0 \leqslant t \leqslant 300$) and (b) a long time scale ($0 \leqslant t \leqslant 6000$) are shown. The growth rates for even and odd harmonics are given by $\gamma_{even} \sim 0.12$ and $\gamma_{odd} \sim 0.003$, respectively. Time evolution of the entropy is also illustrated as a reference.

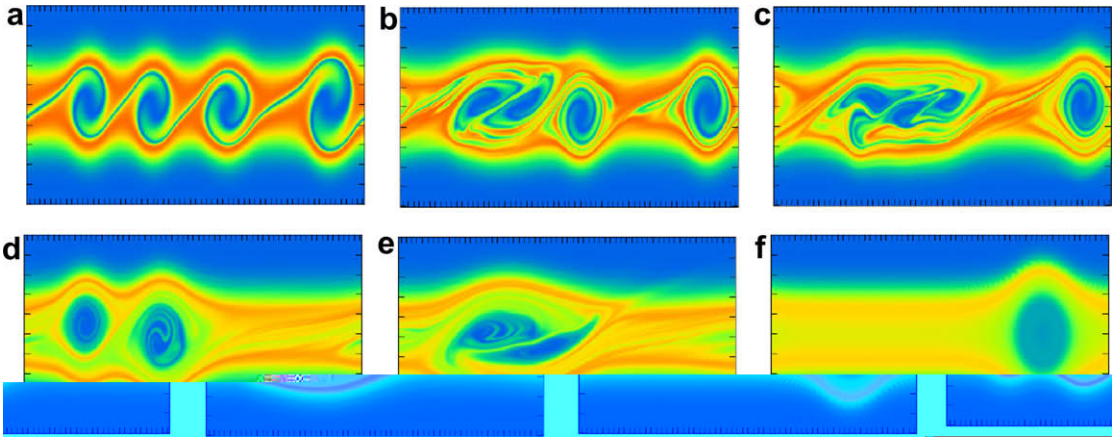

Fig. 19. Contour plots of the distribution function (linear plot) in phase space at six different snap times: (a) $t = 40$, (b) $t = 60$, (c) $t = 80$, (d) $t = 180$, (e) $t = 200$ and (f) $t = 6000$, in case-2. The domain $R = \{(x, v)\,|\,|x| \leqslant 10\pi, |v| \leqslant 5\}$ is illustrated.

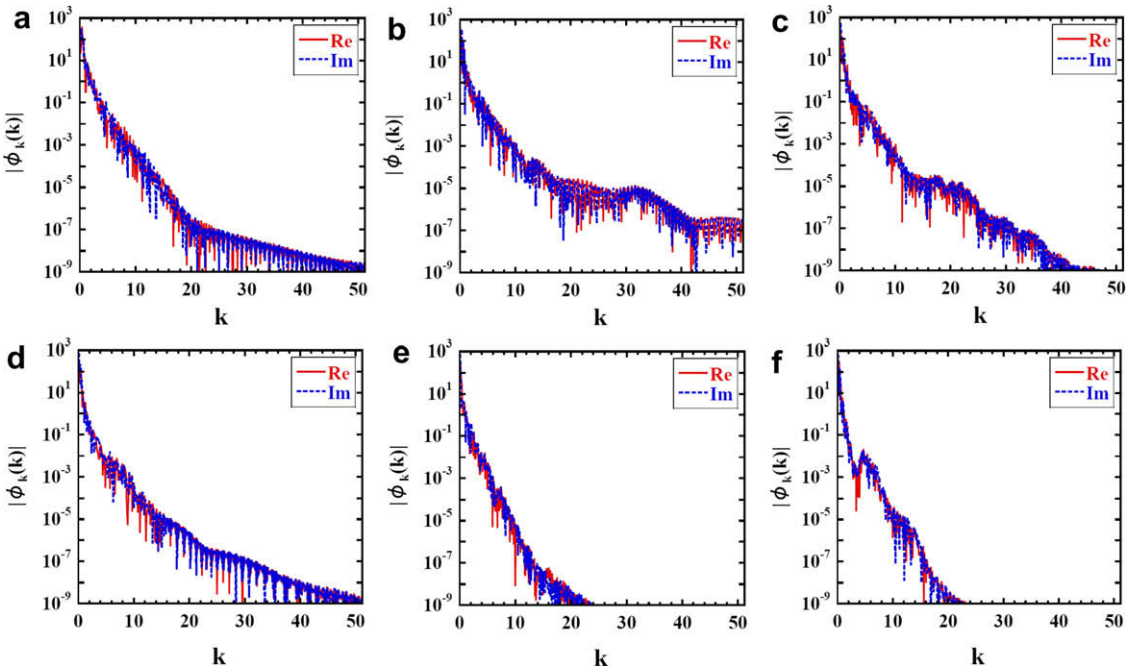

Fig. 20. Spectral distributions of the electrostatic potential $\phi(x)$ at six different snap times: (a) $t = 40$, (b) $t = 60$, (c) $t = 80$, (d) $t = 180$, (e) $t = 200$ and (f) $t = 6000$, in case-2. A real part and imaginary part, which correspond to even and odd harmonics, respectively, are shown.

the conservation of the L1-norm is found to be drastically improved so that it is kept at almost a constant value, as seen in Fig. 21(b). This is due to the fact that the fine scale structure originating from the trapping motion near the separatrix is coarse-grained by the collisional effect. In other words, in this case, collisional dissipation which is physically determined overcomes the numerical one. This can be seen from Fig. 21(c2) where the entropy starts to increase at $t = \tau_{CE} \sim 5$, which is earlier than that in the $\beta = 0$ case, i.e., $t = \tau_{NE} \sim 20$.

4.2. Numerical simulations of the 4D Vlasov–Poisson system in phase space

Here, we have extended to the 4D Vlasov–Poisson equation system in phase space which is given by a normalized form

$$\frac{\partial f}{\partial t} + \frac{\partial (v_x f)}{\partial x} + \frac{\partial (v_y f)}{\partial y} - \frac{\partial (E_x(t,x,y) f)}{\partial v_x} - \frac{\partial (E_y(t,x,y) f)}{\partial v_y} = 0, \tag{57}$$

$$\frac{\partial E_x(t,x,y)}{\partial x} + \frac{\partial E_y(t,x,y)}{\partial x} = -\left\{ \int_{-\infty}^{\infty} \int_{-\infty}^{\infty} f \, dv_x \, dv_y - 1 \right\}, \tag{58}$$

where the distribution function has four independent variables in phase space as $f = f(t,x,y,v_x,v_y)$. This model has been tested in some literatures [15,23,24] as a high dimensional case. The IDO-CF scheme can be directly applied to such a simulation by following the same numerical procedure as in the 2D case since Eqs. (57) and (58) are the same as Eqs. (14) and (15) in the form. Following the discussion by Ref. [15,23,24], we set the initial condition as,

$$f(t=0,x,y,v_x,v_y,t) = \frac{1}{2\pi}\exp\left(-\frac{v_x^2+v_y^2}{2}\right)\left\{1+B\left(\cos\frac{2\pi}{L_x}x + B\cos\frac{2\pi}{L_y}y\right)\right\}. \tag{59}$$

The computational domain $R = \{(x,y,v_x,v_y)\,|\,0 \leqslant x \leqslant 4\pi, 0 \leqslant y \leqslant 4\pi, |v_x| \leqslant 7, |v_y| \leqslant 7\}$ is uniformly discretized with $32\times32\times128\times128$ meshes, and the time-step size is set as $\Delta t = 1/40$. In this case, the evolutions of $E_x(k_x,k_y)$ and $E_y(k_x,k_y)$ are identical due to the initial symmetry. First, we consider the linear Landau damping where $B = 0.05$ is given as the initial parameter. In Fig. 22, the time evolution of the amplitude of the Fourier mode $E_y(k_=0.5, k_y = 0)$ is plotted in logarithmic scale obtained by using the Spline and IDO-CF2 scheme. The IDO-CF scheme gives an accurate damping of the amplitude of the electric field, showing that the damping rate is in good agreement with the theoretical value ($\gamma = 0.1533$).

Then, the nonlinear Landau damping is considered by setting $B = 0.5$. The time histories of the field energy and total energy obtained by using both schemes are shown in Figs. 23 and 24, respectively. Fig. 23 shows that the time evolution of the field energy is in good agreement with the results given in the literatures, i.e., the exponential damping of initial electrostatic field perturbation and subsequent growth. Most importantly, the IDO-CF2 scheme has superior in preserving conservation property for the total energy in high dimensional case, especially in linear phase as shown in Fig. 24. The mass conservation is rigorously kept in the order of 10^{-15}. These properties are almost the same as in the 2D case.

4.3. Numerical simulations of the guiding-center drift equation system in real space

So far, we have applied the IDO-CF scheme in the 2D Vlasov system with (x, v_x), which is of minimum dimensionality in phase space. However, there is no essential difference in extending the method to higher dimensional case such as 4D and 6D as discussed in Section 4.2. Meanwhile, in the drift-kinetic and/or gyro-kinetic formalisms, which are efficient approaches in describing complex plasma dynamics in strong magnetic field, the velocity $\vec{v}$ is no longer independent variable, but depends on spatial coordinates through electric field and also magnetic field such as $\vec{E}\times\vec{B}$ and $\vec{\nabla}B\times\vec{B}$ drift motion. In this case, the semi-Lagrangian approach is hardly applied since the time splitting cannot be introduced. On the other hand, the IDO-CF scheme is based on Eulerian approach so that it can be directly applied to such a simulation. As a benchmark test, we consider the 2D guiding-center equation given by

$$\frac{\partial f(t,x,y)}{\partial t} - \frac{\partial\phi(t,x,y)}{\partial y}\frac{\partial f(t,x,y)}{\partial x} + \frac{\partial\phi(t,x,y)}{\partial x}\frac{\partial f(t,x,y)}{\partial y} = 0, \tag{60}$$

where ρ and ϕ denote the density and the electrostatic potential, respectively, which satisfy the Poisson equation,

$$\frac{\partial^2\phi(t,x,y)}{\partial x^2} + \frac{\partial^2\phi(t,x,y)}{\partial x^2} = -\rho. \tag{61}$$

Note that the convection terms in Eq. (60) can be rewritten as the conservative form as $-\partial/\partial x(\rho\partial\phi/\partial y) + \partial/\partial y(\rho\partial\phi/\partial x)$ so that the IDO-CF scheme can be easily applied to this system. Following the discussion by Shoucri [29], we set the initial condition as

$$\rho(t=0,x,y) = \sin y + \epsilon\sin\frac{y}{2}\cos(k_1 x). \tag{62}$$

This expression represents a shear flow in the x-direction and then Kelvin–Helmholtz (K–H) instability may be excited. The simulation domain $R = \{(x,y)\,|\,0 \leqslant x \leqslant 10, 0 \leqslant y \leqslant 2\pi\}$ is uniformly discretized with mesh numbers 256×256, and the time-step size is set as $\Delta t = 5.0\times10^{-2}$. The fixed boundary condition with zero density and potential is employed in the y-direction, i.e, $\rho = \phi = 0$ at $y = 0, 2\pi$, while periodic boundary condition in the x-direction. In this case, the linear growth rate is approximately solved as

$$\frac{Im(\omega)}{k} = \frac{\sqrt{3}}{2}\left(\frac{\sqrt{3}}{2} - k_1\right). \tag{63}$$

We have performed the simulation with the same initial parameters as that employed in Ref. [22,30], that is, $\epsilon = 0.05$ and $k_1 = 2\pi/L_x = 2\pi/10$.

At first, we have investigated the linear growth rate of the density perturbation for the most unstable wave number, i.e., $k = k_1$ by using the Arakawa and present IDO-CF schemes. The Arakawa scheme [31] is a well-known FDM for the integration of the Euler equation for 2D fluid flows, which conserves both mean energy and mean square vorticity. In the present study, these values correspond to enstrophy and field energy, respectively. The linear growth rate in both schemes is given by $\gamma \simeq 0.114$, which is in good agreement with that obtained in Ref. [32] ($\gamma \simeq 0.113$). It is also consistent with the analytical estimate given by Eq. (63) ($\gamma \simeq 0.129$).

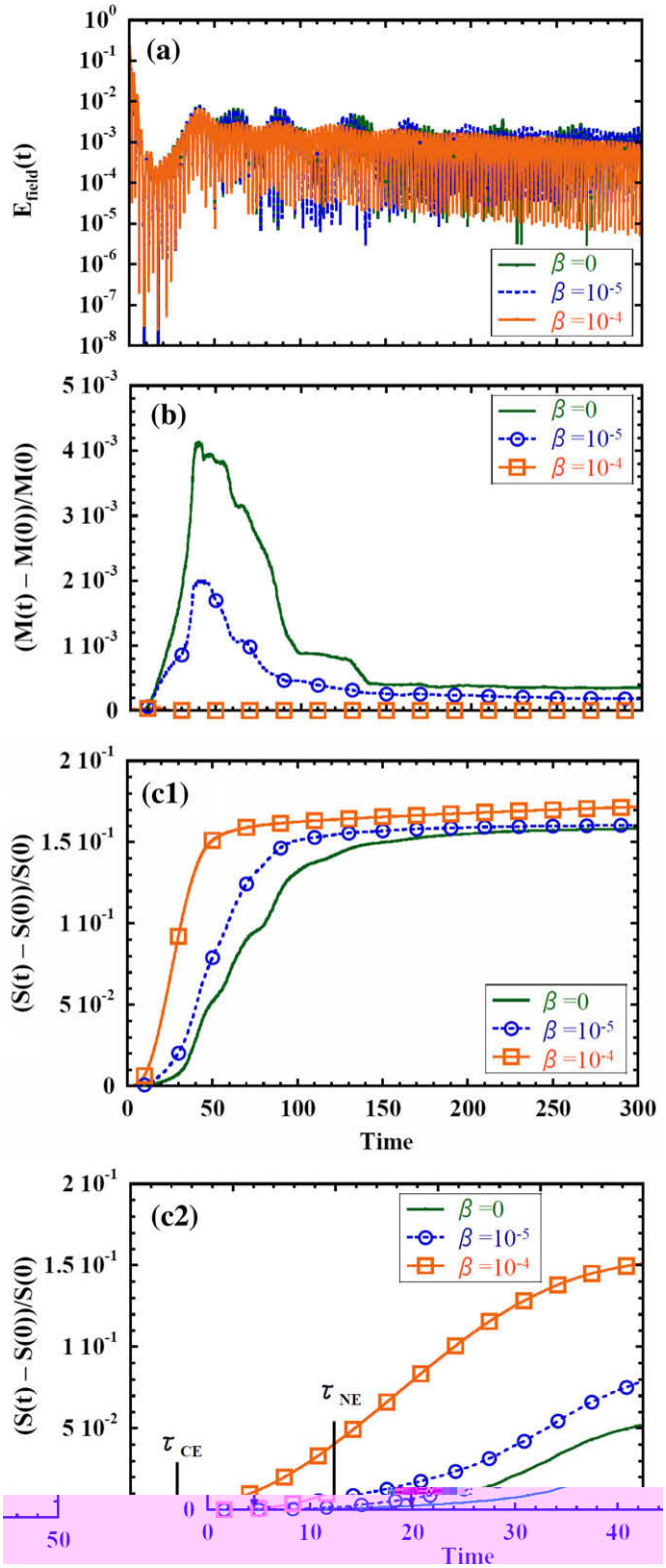

Fig. 21. Time evolutions of (a) field energy, (b) L1-norm and (c1, c2) entropy for different collisional frequency β for IDO-CF2 scheme. (c1) and (c2) correspond to a long time scale ($0 \leqslant t \leqslant 300$) and a short time one ($0 \leqslant t \leqslant 50$), respectively.

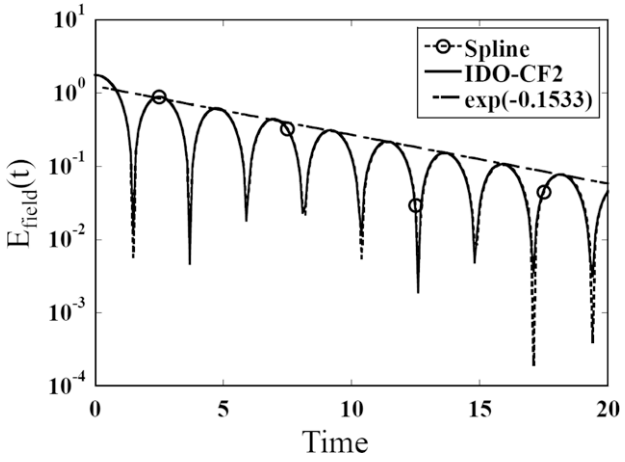

Fig. 22. Time evolutions of field energy in the linear Landau damping case for the Spline and IDO-CF2 scheme. Theoretical damping rate ($\gamma = 0.1533$) is also shown as a reference.

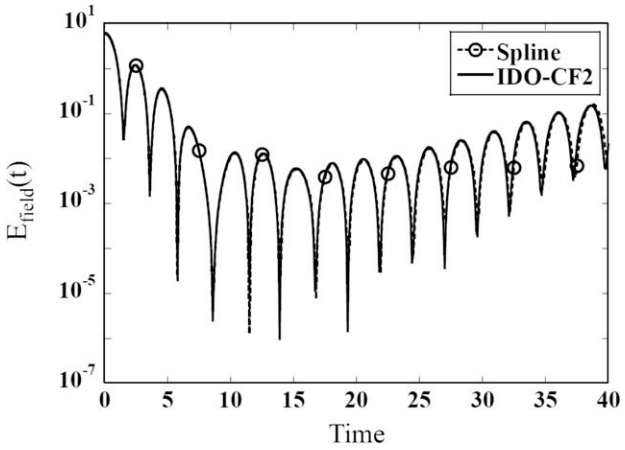

Fig. 23. Time evolutions of field energy in the nonlinear Landau damping case for the Spline and IDO-CF2 scheme.

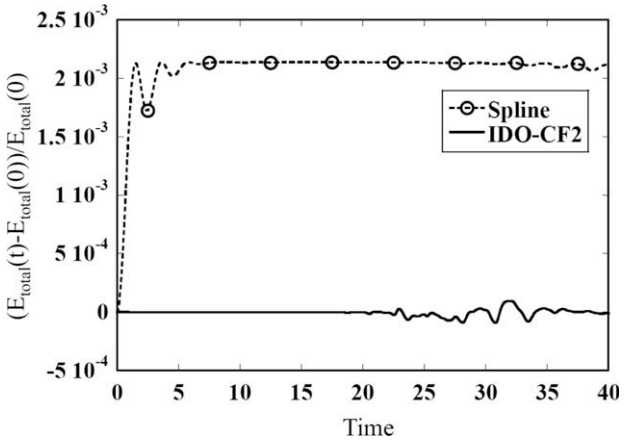

Fig. 24. Time evolutions of the relative total energy error in the nonlinear Landau damping case for the Spline and IDO-CF2 scheme.

The time histories of the field energy $\int\int |\vec{\nabla}\phi|^2 dx\,dy$, which is the conserved quantity of the system, is shown in Fig. 25. The error of the field energy after the saturation is about 6×10^{-4}, which is almost the same in both cases since the error dominantly originates from the Poisson solver. On the other hand, the enstrophy is conserved in the Arakawa scheme,

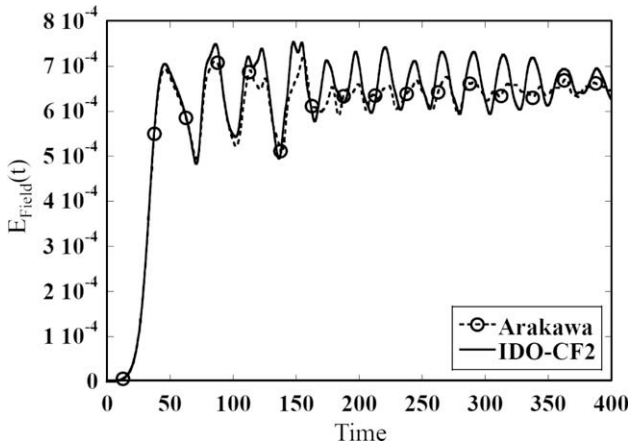

Fig. 25. Time evolutions of the relative field energy error in the K–H instability for the Arakawa and IDO-CF2 scheme.

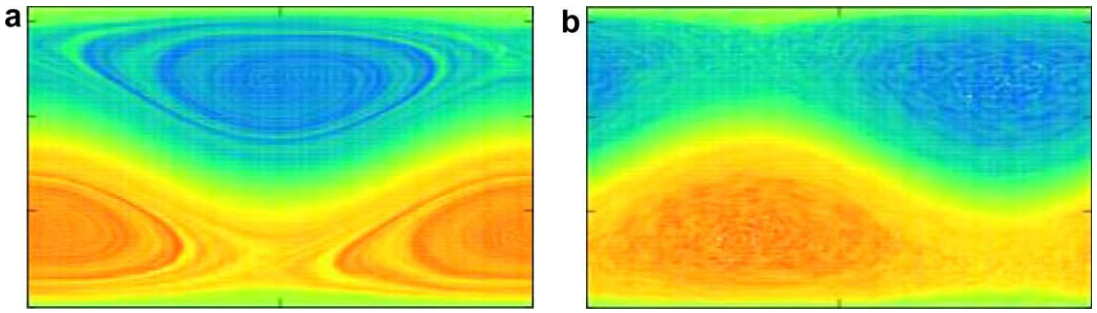

Fig. 26. Contour plots of the density at (a) $t = 100$, (b) $t = 400$ for the Arakawa scheme. The domain $R = \{(x,y)|0 \leqslant x \leqslant 10, 0 \leqslant y \leqslant 2\pi\}$ is illustrated.

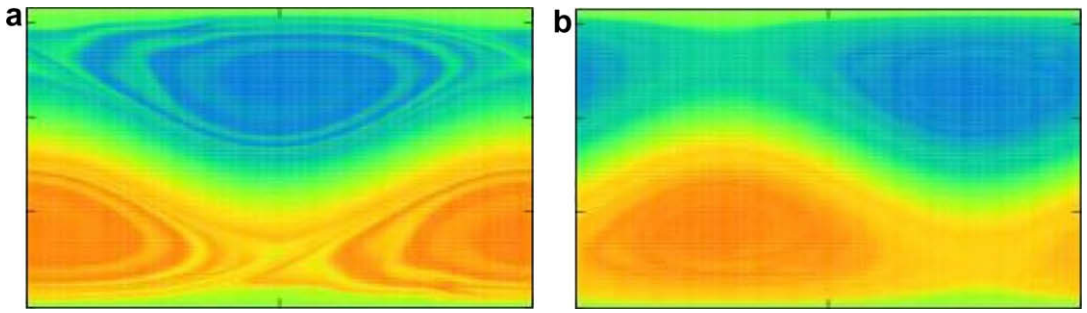

Fig. 27. Contour plots of the density at (a) $t = 100$, (b) $t = 400$ for the IDO-CF2 scheme. The domain $R = \{(x,y)|0 \leqslant x \leqslant 10, 0 \leqslant y \leqslant 2\pi\}$ is illustrated.

suggesting that the scheme is non-dissipative. Due to this property, no damping takes place even near the Nyquist wave number, leading to the Gibbs oscillation [34]. The IDO-CF scheme can keep the enstrophy almost constant up to the end of linear phase, however it starts to grow in nonlinear phase due to the dissipation to high-k components. The relative error of the enstrophy is about 3×10^{-2} in the equilibrium state.

The contour plots of the density at (a) $t = 100$ and (b) $t = 400$ for the Arakawa and IDO-CF schemes are shown in Figs. 26 and 27, respectively. The corresponding density cross sections at $x = 5$ are also shown in Fig. 28(a) and (b). Small scale corrugation can be observed in the Arakawa scheme. This originates from the non-dissipative high-k components which accumulate near the Nyquist wave number. This phenomena also appears in the 2D Vlasov simulation in phase space. Although the Arakawa scheme preserves the conservation properties as Hamiltonian system, it does not ensure the positivity of distribution function, i.e., $f > 0$ due to the inevitable phase errors at moderate $k\Delta x$ and cause the Gibbs oscillation in the case without collision. In the present case, such an oscillation does not lead to fatal numerical instability, but small scale corrugations are unphysically produced. The IDO-CF scheme based on the upwind discretization includes numerical dissipation

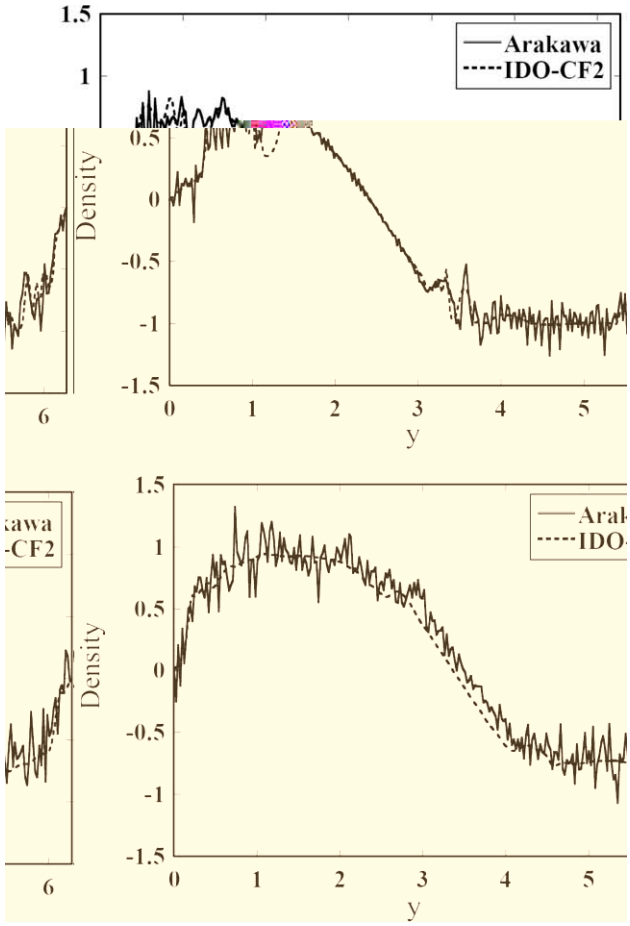

Fig. 28. Cross sections of the density at $x = 5$ for the Arakawa and IDO-CF2 schemes. Two different times, (a) $t = 100$, (b) $t = 400$ are shown.

for high-k components, however, fine scale structure up to moderate wave number region can be properly captured with negligibly small phase error.

5. Conclusions

In this paper, we have introduced the conservation form of the IDO (IDO-CF) scheme in order to solve the Vlasov–Poisson equation which describes various linear and nonlinear plasma dynamics. The IDO-CF scheme is one of the multi-moment schemes, and has an advantage in extending the simulation with dissipation and also source/sink terms, which are essential for long time scale simulation. We have applied this scheme to calculate the nonlinear Landau damping and two-stream instability as numerical tests. As measures characterizing the numerical accuracy, we have investigated the conservation properties of the L1-norm, energy, entropy and phase space area for different schemes, i.e., the Spline, CIP and IDO-CF ones. We have paid particular attention to the entropy, which is a measure of higher order moment related to a fine scale structure.

The IDO-CF2 scheme, which is a strict version for evaluating the line-integrated values ρ, ζ and the cell-integrated value M, was found to be suitable for long time scale simulation of the nonlinear dynamics with no serious numerical instability. The energy conservation of the IDO-CF2 scheme is better than that of the other schemes, whereas the L1-norm is also well conserved in the IDO-CF2 scheme together with the CIP and IDO-CF1 schemes. On the other hand, the entropy and phase space area increase by a certain amount in all schemes during the saturation of linear instability and subsequent trapping process. This originates from the ergotization of the fine scale structure near the separatrix due to small numerical dissipation. Through this process, a coarse-grained distribution function is established. Then, the entropy and phase space area saturate and tend to converge to asymptotic values. This state is understood to be a quasi-stable BGK solution.

In order to study how the microscopic resolution influences the macroscopic dynamics, we have investigated the symmetry of the distribution function, which is one of the most primitive macroscopic properties, by artificially imposing a symmetry constraint to the initial perturbation of the distribution function. We found that the entropy increases when

complex merging of vortices takes place, but the symmetric structure is kept even after this process. However, we also found that such a symmetric BGK distribution becomes unstable for the perturbations of odd harmonics, so that the small numerical noise triggered during the ergotization process ultimately causes a symmetry breaking of the distribution function. However, it should be noted that the observed secondary instability and associated merging are considered to be deterministic without regard to the scheme.

As applications of the IDO-CF scheme to particular problems in plasmas, first we have performed a simulation with the linear collision term, i.e., a Fokker–Planck simulation. As the increase of collision frequency, the production rate of the entropy, which is physically determined, also increases so that the entropy production due to the numerical dissipation is masked. Resultantly, the conservation of the L1-norm is found to be drastically improved since the fine scale structure becomes coarse-grained by collision faster than by numerical dissipation. Then we have performed the 4D Vlasov–Poisson simulation in phase space, and found that the IDO-CF2 scheme gives an accurate damping of the electric field. The scheme is superior in preserving conservation properties for the total mass and energy in high dimensional case. These properties are almost the same as in the 2D case. Finally, the 2D guiding-center drift simulation in real space has been performed. The IDO-CF scheme still has good conservation properties for the field energy and enstrophy, and can properly capture fine scale structure up to moderate wave number region with less phase error. From these applications, it is considered that the IDO-CF scheme can be extended to more realistic simulation such as gyrokinetic Vlasov simulation [5–8] which will be reported in a future publication.

Acknowledgements

The authors sincerely thank Prof. T. Aoki of Tokyo Institute of Technology for his variable discussions and comments. This work was supported by the Grant-in-Aid from JSPS (Grant Nos. 21340171 and 19560828) and also by Kyoto University Global COE Program (Energy Science in the Age of Global Warming).

References

[1] R.C. Davidson, Methods in Nonlinear Plasma Theory, Academic Press, New York, 1972.
[2] S. Ichimaru, Statistical Plasma Physics: Basic Principles, Addison-Wesley, Redwood City, 1992.
[3] C.K. Birdsall, A.B. Langdon, Plasma Physics via Computer Simulation, Adams Hilger, Bristol, 1991.
[4] T. Tajima, Computational Plasma Physics: With Applications to Fusion and Astrophysics, Addison-Wesley, Redwood City, 1989.
[5] F. Jenko, Massively parallel Vlasov simulation of electromagnetic drift-wave turbulence, Comput. Phys. Commun. 125 (2000) 196.
[6] T.-H. Watanabe, H. Sugama, Kinetic simulation of a quasisteady state in collisionless ion temperature gradient driven turbulence, Phys. Plasmas 9 (2002) 3659.
[7] J. Candy, R.E. Waltz, An Eulerian gyrokinetic-Maxwell solver, J. Comput. Phys. 186 (2003) 545.
[8] Y. Idomura, M. Ida, S. Tokuda, L. Villard, New conservative gyrokinetic full-f Vlasov code and its comparison to gyrokinetic δf particle-in-cell code, J. Comput. Phys. 226 (2007) 244.
[9] M. Shoucri, Eulerian codes for the numerical solution of the Vlasov equation, Commun. Nonlinear Sci. Numer. Simul. 13 (2008) 174.
[10] T. Umeda, M. Ashour-Abdalla, D. Schriver, Comparison of numerical interpolation schemes for one-dimensional electrostatic Vlasov code, J. Plasma Phys. 72 (2006) 1057.
[11] C.Z. Cheng, G. Knorr, The integration of the Vlasov equation in configuration space, J. Comput. Phys. 22 (1976) 330.
[12] H. Yoshida, Construction of higher order symplectic integrators, Phys. Lett. A 150 (1990) 262.
[13] T. Yabe, F. Xiao, T. Utsumi, The constrained interpolation profile method for multiphase analysis, J. Comput. Phys. 169 (2001) 556.
[14] T. Utsumi, T. Kunugi, T. Aoki, Stability and accuracy of the cubic interpolated propagation scheme, Comput. Phys. Commun. 101 (1997) 9.
[15] T. Nakamura, T. Yabe, Cubic interpolated propagation scheme for solving the hyper-dimensional Vlasov–Poisson equation in phase space, Comput. Phys. Commun. 120 (1999) 122.
[16] T.-H. Watanabe, H. Sugama, T. Sato, A nondissipative simulation method for the drift kinetic equation, J. Phys. Soc. Jpn. 70 (2001) 3565.
[17] T. Aoki, Interpolated Differential Operator (IDO) scheme for solving partial differential equations, Comput. Phys. Commun. 102 (1997) 132.
[18] Y. Imai, T. Aoki, Accuracy study of the IDO scheme by Fourier analysis, J. Comput. Phys. 217 (2006) 453.
[19] Y. Imai, T. Aoki, Stable coupling between vector and scalar variables for the IDO scheme on collocated grids, J. Comput. Phys. 215 (2006) 81.
[20] Y. Imai, T. Aoki, K. Takizawa, Conservative form of interpolated differential operator scheme for compressible and incompressible fluid dynamics, J. Comput. Phys. 227 (2008) 2263.
[21] M. Zerroukat, N. Wood, A. Staniforth, The Parabolic Spline Method (PSM) for conservative transport problems, Int. J. Numer. Meth. Fluids 51 (2006) 1297.
[22] T.-H. Watanabe, H. Sugama, Vlasov and drift kinetic simulation methods based on the symplectic integrator, Transport Theory Statist. Phys. 34 (2005) 287.
[23] F. Filbet, E. Sonnendrücker, P. Bertand, Conservative numerical schemes for the Vlasov equation, J. Comput. Phys. 172 (2001) 166.
[24] F. Filbet, E. Sonnendrücker, Comparison of Eulerian–Vlasov solvers, Comput. Phys. Commun. 150 (2003) 247.
[25] G.M. Zaslavskii, B.V. Chirikov, Stochastic instability of nonlinear oscillations, Sov. Phys. Usp. 14 (1972).
[26] L. Galeotti, F. Califano, Asymptotic evolution of weakly collisional Vlasov–Poisson plasmas, Phys. Rev. Lett. 95 (2005) 015002.
[27] F. Califano, L. Galeotti, A. Mangeney, The Vlasov–Poisson model and the validity of a numerical approach, Phys. Plasmas 13 (2006) 082102.
[28] T. Utsumi, T. Kunugi, J. Koga, A numerical method for solving the one-dimensional Vlasov–Poisson equation in phase space, Comput. Phys. Commun. 108 (1998) 159.
[29] M. Shoucri, A two-level implicit scheme for the numerical solutions of the linearized vorticity equation, Int. J. Numer. Meth. Eng. 17 (1981) 1525.
[30] E. Sonnendrücker, J. Roche, P. Bertrand, A. Ghizzo, The semi-Lagrangian method for the numerical resolution of the Vlasov equation, J. Comput. Phys. 149 (1999) 201.
[31] A. Arakawa, Computational design for long-term numerical integration of the equation of fluid motion: Two-dimensional incompressible flow. Part 1, J. Comput. Phys. 1 (1) (1966) 119.
[32] G.W. Hammett, J.L. Peterson, Positivity-preserving algorithms for continuum gyrokinetic and gyrofluid simulations of edge plasma turbulence, Bull. Am. Phys. Soc. 53 (2008) 276.